

# Ice thickness and bed topography of Jostedalsbreen ice cap, Norway

Mette K. Gillespie<sup>1</sup>, Liss M. Andreassen<sup>2</sup>, Matthias Huss<sup>3,4,5</sup>, Simon de Villiers<sup>1</sup>, Kamilla H. Sjurssen<sup>1</sup>, Jostein Aasen<sup>2</sup>, Jostein Bakke<sup>6</sup>, Jan M. Cederstrøm<sup>6</sup>, Hallgeir Elvehøy<sup>2</sup>, Bjarne Kjøllmoen<sup>2</sup>, Even Loe<sup>7</sup>, Marte Meland<sup>8</sup>, Kjetil Melvold<sup>2</sup>, Sigurd D. Nerhus<sup>1</sup>, Torgeir O. Røthe<sup>1</sup>, Eivind W. N. Støren<sup>6,9</sup>, Kåre Øst<sup>10</sup>, Jacob C. Yde<sup>1</sup>

<sup>1</sup>Department of Civil Engineering and Environmental Sciences, Western Norway University of Applied Sciences, Sogndal, 6851, Norway

<sup>2</sup>Section for Glaciers, Ice and Snow, Norwegian Water Resources and Energy Directorate (NVE), Oslo, 0301, Norway

<sup>3</sup>Laboratory of Hydraulics, Hydrology and Glaciology (VAW), ETH Zurich, Zurich, 8092, Switzerland

<sup>4</sup>Swiss Federal Institute for Forest, Snow and Landscape Research (WSL), Birmensdorf, CH-8903, Switzerland

<sup>5</sup>Department of Geosciences, University of Fribourg, Fribourg, 1700, Switzerland

<sup>6</sup>Department of Earth Science and the Bjerknes Centre for Climate Research, University of Bergen, 5020, Norway

<sup>7</sup>Statkraft, Gaupne, 6868, Norway

<sup>8</sup>Breheimsenteret, Jostedal, 6871, Norway

<sup>9</sup>COWI, Bergen, 5824, Norway

<sup>10</sup>Norgesguidene, Jostedal, 6871, Norway

*Correspondence to:* Mette Kusk Gillespie (mette.kusk.gillespie@hvl.no)

**Abstract.** We present an extensive dataset of ice thickness measurements from Jostedalsbreen ice cap, mainland Europe's largest glacier. The dataset consists of more than 351 000 point values of ice thickness distributed along ~1100 km profile segments that cover most of the ice cap. Ice thickness was measured during field campaigns in 2018, 2021, 2022, and 2023 using various ground-penetrating radar (GPR) systems with frequencies ranging between 2.5 and 500 MHz. The large majority of ice thickness observations were collected in spring using either snowmobiles (90 %) or a helicopter-based radar system (8 %), while summer measurements were carried out on foot (2 %). To ensure accessibility and ease of use, metadata were attributed following the GlaThiDa dataset (GlaThiDa Consortium, 2020) and follows the FAIR (Findable, Accessible, Interoperable, and Reusable) guiding principles. Our findings show that glacier ice of more than 400 m thickness is found in the upper regions of large outlet glaciers, with a maximum ice thickness of ~630 m in the accumulation area of Tunsbergdalsbreen. Thin ice of less than 50 m covers narrow regions joining the central part of Jostedalsbreen with its northern and southern parts, making the ice cap vulnerable to break-up with future climate warming. Using the point values of ice thickness as input to an ice thickness model, we compute 10 m grids of ice thickness and bed topography that cover the entire ice cap. From these distributed datasets we find that Jostedalsbreen (458 km<sup>2</sup> in 2019) has a present (~2020) mean ice thickness of 154 m ±22 m and an ice volume of 70.6 ±10.2 km<sup>3</sup>. Locations of depressions in the map of bed topography are used to delimitate the locations of potential future lakes, consequently providing a glimpse of

36 the landscape if the entire Jostedalsbreen melts away. Together, the comprehensive ice thickness point values  
37 and ice cap-wide grids serve as a baseline for future climate change impact studies at Jostedalsbreen. All data are  
38 available for download at <https://doi.org/10.58059/yhwr-rx55> (Gillespie et al., 2024).

## 39 **1 Introduction**

40 Global glacier mass loss caused by increased atmospheric temperatures and associated processes contributes  
41 significantly to changes in sea level, water resources and natural hazards (IPCC, 2021). Projections of future  
42 changes show that glaciers and ice caps will continue to lose mass due to anthropogenic warming, and that the  
43 majority of the world's glaciers and ice caps are at risk of being lost by 2100 (Rounce et al., 2023). However, global  
44 glacier projections remain uncertain. This is especially true for ice caps, where model efforts of ice thickness  
45 distribution in the flat upper regions and across ice divides represents a particular challenge (Millan et al., 2022;  
46 Frank et al., 2023).

47  
48 Information on ice thickness distribution of a glacier is a prerequisite for accurate modelling of ice dynamics and  
49 glacier evolution, as well as future hydrological impacts. Ice thickness measurements are also essential for precise  
50 calculations of the ice volume of glaciers and in mapping of the subglacial topography. Consequently, significant  
51 efforts have been made to compile ice thickness data and provide grids of ice thickness and bed topography (e.g.,  
52 Gärtner-Roer et al., 2014; Lindbäck et al., 2018; Frémand et al., 2023). The third version of the Glacier Thickness  
53 Database (GlaThiDa v3) includes nearly 4 million ice thickness measurements distributed over roughly 3000  
54 glaciers worldwide, and 14 % of the world's glacierized area is now within 1 km of an ice thickness measurement  
55 (GlaThiDa Consortium, 2020; Welty et al., 2020). Direct inter- and extrapolation of ice thickness measurements  
56 with various techniques, such as kriging, inverse-distance weighting, or spline interpolations (Flowers and Clarke,  
57 1999; Binder et al., 2009; Fischer, 2009; Yde et al., 2014; Andreassen et al., 2015) is possible, but may produce  
58 large uncertainties in areas without measurements (Gillespie et al., 2023). Consequently, ice thickness modelling  
59 is necessary to extrapolate measurements more accurately to unmeasured regions (Andreassen et al., 2015;  
60 Farinotti et al., 2021), and to infer ice thickness for glaciers without direct measurements.

61  
62 Various ice thickness inversion approaches exist that do not require bed topography or ice thickness as input (e.g.,  
63 Huss and Farinotti et al., 2012; Linsbauer et al., 2012;; Farinotti et al., 2019; Frank et al., 2023), and recent efforts  
64 to model ice thickness through inversion of surface topography have made distributed ice thickness information  
65 available for every individual glacier in the world (Farinotti et al, 2019; Millan et al., 2022) and all Scandinavian  
66 glaciers and ice caps (Frank and van Pelt, 2024). Although ice thickness observations are not required as input in  
67 these models, databases of ice thickness, when available, remain important for calibration and validation of model

68 behaviour. Assessments of model performances, such as the first Ice Thickness Model Intercomparison  
69 eXperiment (ITMIX; Farinotti et al., 2017), found that model output is highly variable, and that the best results are  
70 achieved when using model ensembles. In addition, a more recent model comparison (ITMIX2; Farinotti et al.,  
71 2021) demonstrated the added value of in situ ice thickness observations to constrain models. A limited set of ice  
72 thickness observations, preferably from the thickest parts of the glacier, were efficient to constrain mean glacier  
73 thickness, illustrating that even sparse ice thickness observations are of importance in ice thickness modelling.  
74 Consequently, readily accessible ice thickness observations for calibration and validation remain key for developing  
75 a new generation of ice thickness estimation models (Farinotti et al., 2017).

76

77 In Norway, numerous field campaigns to measure ice thickness have been carried out over the years (Andreassen  
78 et al., 2015). The purpose of the earliest measurements was typically to determine subglacial topography in relation  
79 to hydropower planning, such as subglacial intakes and water divides (e.g., Kennett, 1989, 1990), or detailed  
80 studies related to jökulhlaups (Engeset et al., 2005). While the first attempts at ice thickness mapping used seismic  
81 measurements (e.g., Sellevold and Kloster, 1964) or hot water drilling (e.g., Østrem et al., 1976), from 1980,  
82 ground-penetrating radar (GPR) has been the preferred method for largescale mapping of glaciers in Norway (e.g.,  
83 Sætrang and Wold, 1986).

84

85 Since these first radar measurements on Norwegian glaciers, technological advancements in radar systems,  
86 processing techniques and positioning accuracy have enabled the use of GPR in a wide range of glaciological  
87 applications, such as mapping of ice- or snow thickness, internal layering, thermal regime, or englacial meltwater  
88 channels (e.g., Plewes and Hubbard, 2001; Dowdeswell and Evans, 2004; Navarro and Eisen, 2009). The  
89 penetration depth and level of detail in GPR data are determined by the antenna frequency. Information on ice and  
90 snow characteristics can be achieved by using very-high (30–300 MHz) or ultra-high (300–3000 MHz) antenna  
91 frequencies, while high-frequency GPR surveys (3–30 MHz antenna frequency) have larger penetration depth at  
92 the expense of resolution (Schlegel et al., 2022). High-frequency antennas are consequently the better choice in  
93 surveys of bed topography, and grids of glacier geometry based on such measurements have been widely used to  
94 model future changes in Norwegian glaciers (e.g., Laumann and Nesje, 2009, 2014; Giesen et al., 2010; Åkesson  
95 et al., 2017, Johansson et al., 2022).

96

97 Jostedalbreen is the largest ice cap in mainland Europe and makes up about 20 % of the total glacierized area of  
98 mainland Norway (Andreassen et al., 2022). The effect of global warming is evident in the region and monitored  
99 outlet glaciers flowing from the ice cap have thinned and retreated with increased speed since 2000 (e.g.,  
100 Andreassen et al., 2020; Seier et al., 2024). The effects of future warming on accessibility, glacier-atmosphere  
101 systems and hydrology are likely to significantly impact regional businesses such as agriculture, tourism, and

102 hydropower companies. Despite the importance of Jostedalsbreen to both regional stakeholders and the scientific  
103 community, the natural and societal consequences of climate-forced changes in the region remain largely unknown.  
104 Future changes of Jostedalsbreen can be assessed through glacier evolution modelling, but accurate results  
105 require high-quality information on ice thickness and bed topography as model input (Farinotti et al., 2017).  
106 Although several surveys of ice thickness were conducted on Jostedalsbreen during the 1970s and 1980s (e.g.,  
107 Østrem et al., 1976; Andreassen et al., 2015), prior to the new ice thickness measurements described in this paper,  
108 many parts of the ice cap had either poor or no data coverage.

109  
110 Here we present a comprehensive and up-to-date point dataset of ice thicknesses of Jostedalsbreen measured by  
111 GPR during the period 2018–2023. Ice thickness measurements were predominantly performed on the glacier  
112 surface (ground-based), but in regions that were inaccessible on the ground we applied a helicopter (airborne)  
113 radar system. We used antenna frequencies ranging from 2.5 to 500 MHz to capture the thickness of the ice in the  
114 best possible resolution. For regions that remain unmeasured due to resource or accessibility constraints, we use  
115 inter- and extrapolation of the direct measurements in connection with locally constrained ice thickness modelling  
116 to provide new grids of ice thickness and bed topography for the entire ice cap. Depressions in the subglacial bed  
117 topography grid are used to infer the locations of lakes if Jostedalsbreen disappeared completely from the  
118 landscape. We provide a thorough description of the uncertainties associated with ice thickness measurements  
119 and modelling results, including comprehensive uncertainty estimates. The enhanced datasets on Jostedalsbreen  
120 ice thickness and bed topography have the potential to significantly advance modelling efforts for the past and  
121 future evolution of the ice cap and provide accurate assessments of regional climate change impact. In addition,  
122 comprehensive high-accuracy measurements over the complex glacier geometry at Jostedalsbreen constitute a  
123 valuable resource for improving current ice thickness models, particularly on ice caps, where the flat upper regions  
124 and discontinuities across ice divides provide a special challenge.

## 125 **2 Study site**

126 Jostedalsbreen (Fig. 1) has a present (2019) area of 458 km<sup>2</sup> and a surface elevation ranging between 380 and  
127 2006 m a.s.l. (Andreassen et al., 2022). The climate is subarctic to tundra with a mean annual air temperature of -  
128 3°C at 1633 m a.s.l. (2009–2022 average at Steinmannen meteorological station (Fig. 1); Engen et al., 2024). In  
129 the most recent national glacier inventory, Jostedalsbreen is divided into 81 glacier units from observations of  
130 topographic ice divides (Andreassen et al., 2022). Many of these glacier units have individual names which will be  
131 referred to throughout this paper. Jostedalsbreen is defined as a single ice cap but can geographically be divided  
132 into three minor ice caps that are currently connected (Fig. 1). In this paper, we refer to Jostedalsbreen South

133 (south of Grensevarden), Central (north of Grensevarden as far as and including the glacier Lodalsbreen) and  
134 North (northeast of Lodalsbreen).

135

136 Jostedalsbreen reached its maximum Little Ice Age (LIA) extent between 1740 and 1860 CE with an estimated  
137 area of 572 km<sup>2</sup> (Carrivick et al., 2022; Andreassen et al., 2023). Since then, the ice cap has experienced an overall  
138 reduction in size, interrupted temporarily by advances in several fast-responding outlet glaciers, the latest of which  
139 occurred in the 1990s due to increased winter precipitation (Nesje et al., 1995; Andreassen et al., 2005). By 2006,  
140 the major outlet glaciers had in combination lost at least 93 km<sup>2</sup> or 16 % of their LIA area and 14 km<sup>3</sup> or 18 % of  
141 their LIA volume (Carrivick et al., 2022). Increasing summer temperatures further reduced the glacier area by 3 %  
142 between 2006 and 2019 (Andreassen et al., 2022) and continues to do so to this day (Seier et al. 2024). Overall,  
143 the change in the glacial landscape has been considerable, with measurements of glacier front variation (length  
144 changes) at several outlet glaciers revealing a total reduction in length of 1–3 km since ~1900 (Andreassen et al.,  
145 2023), of which 300–700 m has occurred since 2000 (Kjøllmoen et al., 2024).

146

147 The first ice thickness measurements on Jostedalsbreen were conducted in 1973 along two cross profiles located  
148 between 700 and 800 m a.s.l. on the tongue of the outlet glacier Nigardsbreen (Østrem et al., 1976). In total, 14  
149 points were drilled using electrical hot-point drilling, revealing ice thicknesses of up to 200 m. In 1986 hot water  
150 drilling was carried out on the outlet glacier Bødalsbreen along three cross profiles at 780–815 m a.s.l. (Haakensen  
151 and Wold, 1986). Results from 15 boreholes show that ice thickness varied between 50 and 60 m in this region.  
152 GPR was first used on Jostedalsbreen in the 1980s during field campaigns on Nigardsbreen and surrounding  
153 glaciers in 1981, 1984, and 1985 (Sætrang and Wold, 1986), on Austdalsbreen and surrounding glaciers in 1986  
154 (Sætrang and Holmqvist, 1987), and south of Nigardsbreen in 1989 (Andreassen et al., 2015). Results show that  
155 ice thickness along transects typically varied between 150 and 300 m, with ice of up to 600 m in the flattest regions  
156 and thinner ice (50–100 m) at the highest points of the ice cap (Sætrang and Wold, 1986). These early  
157 measurements of ice thickness are associated with relatively large uncertainties in surface elevations and the  
158 positioning of GPR profiles. In addition, as data were collected and processed with analogue techniques, only parts  
159 of the older dataset are available digitally. Digitised data from these campaigns have been submitted to the  
160 GlaThiDa database (GlaThiDa Consortium, 2020; Welty et al., 2020) and were used by Andreassen et al. (2015)  
161 to interpolate ice thickness distribution and estimate a mean ice thickness of 158 m for parts of Jostedalsbreen (65  
162 % of total area). More recently, Jostedalsbreen was included in a modelling study of ice volume and thickness  
163 distribution of all Scandinavian glaciers (Frank and van Pelt, 2024). In this study, Frank and van Pelt (2024) used  
164 ice thickness measurements from the GlaThiDa database (GlaThiDa Consortium, 2020) to calibrate an ice  
165 thickness model, resulting in a total volume of 72.6 km<sup>3</sup> for Jostedalsbreen.

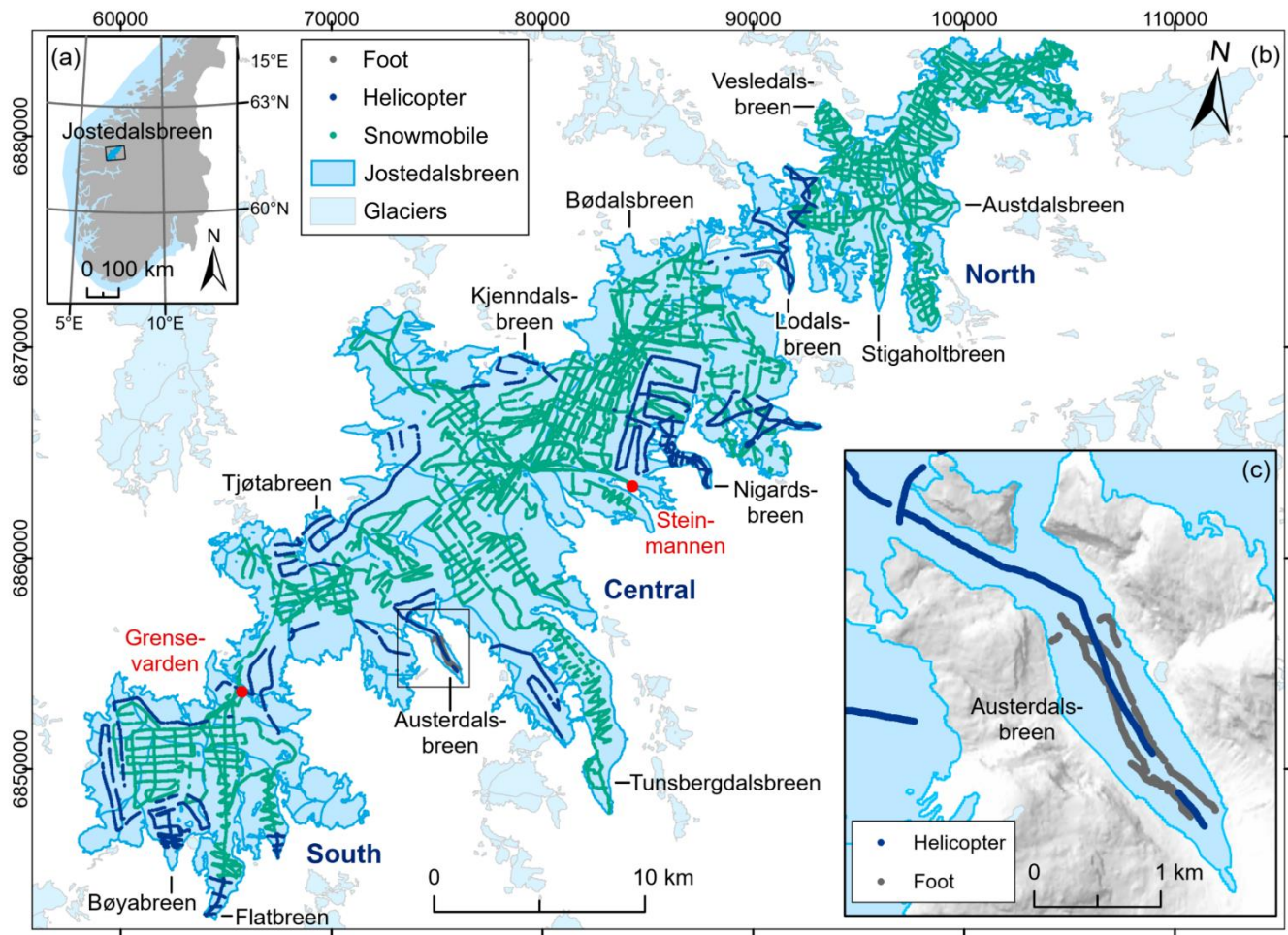
166 **3 Methods and data**

167 **3.1 Ice thickness measurements**

168 The ice thickness measurements presented in this paper were collected during field campaigns between 2018 and  
169 2023. The first measurements were carried out in April 2018, however most of the data were gathered in April  
170 2021, March to April 2022 and April 2023 (Fig. A1a), while the tongue of Austerdalsbreen was surveyed on foot in  
171 September 2021 (Fig. 1c). The principle means of transport during data collection was snowmobile (90 % of all  
172 datapoints), but a new helicopter radar system (Air-IPR) based on the ground-based Blue System Integration Ltd.  
173 IceRadar (Mingo and Flowers, 2010) was deployed for steep and crevassed regions of the ice cap (8 % of all  
174 datapoints). Summer measurements on foot account for only 2 % of all datapoints (Fig. 2). Although airborne  
175 surveys were quicker, ground-based measurements were preferred whenever possible due to the generally better  
176 data quality caused by lower travel speeds, less noise (electronic and off nadir-reflections) and simpler wave  
177 propagation (lack of an air layer). Depending on the surface conditions, we collected the data in a grid pattern, with  
178 the main profiles spaced no more than 400 m apart and oriented transverse to the ice flow direction. Survey lines  
179 perpendicular to main profiles were 400–800 m apart, depending on accessibility and time constrains during the  
180 fieldwork. In total, we have successfully detected the glacier bed along ~920 km of profile segments collected with  
181 the ground-based radar systems and ~170 km of profile segments collected with the airborne radar system (Fig.  
182 1). Following the new measurements, 90 % of the ice cap is now less than 300 m from an observation of ice  
183 thickness (measurement or glacier outline) and 49 % is within 100 m of a known point.

184

185

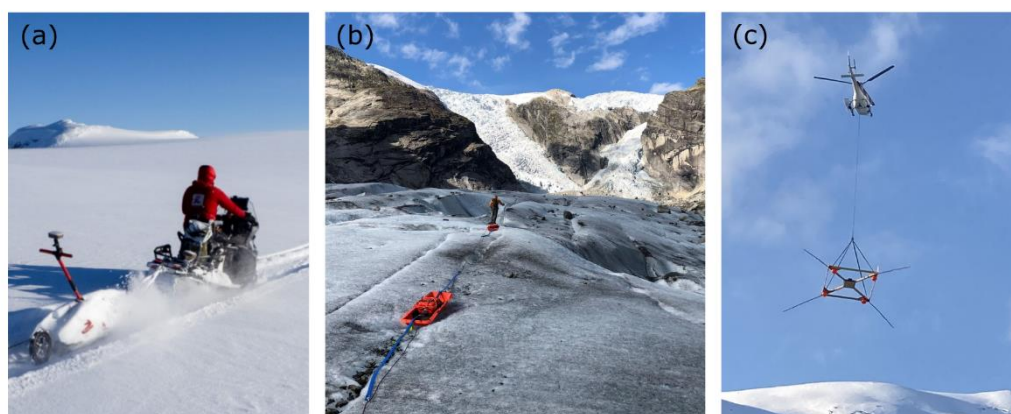


186  
 187 **Figure 1: Map showing (a) the location of Jostedalbreen in southern Norway, (b) Jostedalbreen and GPR surveys**  
 188 **divided into helicopter, snowmobile, and foot, with red dots indicating locations referenced in the text, and (c) the**  
 189 **measurements on Austerdalsbreen by foot and helicopter. The shown glacier extent and outlines of glacier units are**  
 190 **from 2019 (Andreassen et al., 2022). Background mountain shadow on (c) is from the 100 m national DTM by the**  
 191 **Norwegian Mapping Authority. The coordinate systems are geographical coordinates on (a) and UTM 33N, datum**  
 192 **ETRS89 on (b) and (c).**

193  
 194 Based on the terminology proposed by Schlegel et al. (2023), we used a combination of high, very high and ultra-  
 195 high frequency radar systems to gather detailed information on snow, firn and shallow ice, while maintaining a good  
 196 penetration depth for deep ice. Usually two snowmobiles would travel together, one towing a high frequency  
 197 generation 1–3 Blue System Integration Ltd. IceRadar system (Mingo and Flowers, 2010) with 2.5 or 5 MHz  
 198 antennas depending on the ice thickness in the investigated area, and the other snowmobile towing either a higher  
 199 frequency Malå GPR system with 25 or 50 MHz rough terrain antennas, or 450 or 500 MHz shielded antennas  
 200 (Table 1). On one occasion, measurements were conducted using a Radarteam GPR system with a 40 MHz

201 monostatic antenna and an upgraded non-commercial GPR with 5 MHz antennas (NVE-radar), similar to that  
202 described by Sverrisson et al. (1980) and Pettersson et al. (2011). For the measurements on foot on the tongue of  
203 Austerdalsbreen, we chose a 10 MHz Blue System Integration Ltd. IceRadar and a 50 MHz Malå GPR. All  
204 helicopter measurements were collected using a 5 MHz Air-IPR Generation 3 Blue System Integration Ltd.  
205 IceRadar system with the antennas in a V dipole configuration (Table 1). The carrying platform for the Air-IPR is  
206 built with wood and uses telescopic rods in composite material to hold the antennas (Fig. 2c). To ensure a ~30 m  
207 distance between the antennas and the ice surface, we used a laser mounted on the platform with a wireless  
208 connection to the cockpit. Travel speed during the helicopter measurements was  $\sim 10 \text{ m s}^{-1}$  and the control of the  
209 IceRadar during both ground-based and airborne measurements was performed using a tablet and a remote  
210 connection.

211



212

213 **Figure 2: Data collection was undertaken (a) by snowmobile, (b) on foot, and (c) by helicopter. Photos: (a) Kjetil Melvold,**  
214 **(b) Mette K. Gillespie and (c) Torgeir O. Røthe.**

215

216 Ground-based measurements of ice thickness were largely carried out using an in-line antenna configuration with  
217 distances between receiver (Rx) and transmitter (Tx) units depending on the antenna frequency and varying from  
218 4 m (50 MHz) and 6.5 m (25 MHz) for the two Malå rough terrain antennas to 15 m (10 MHz), 30 m (5 MHz) and  
219 60 m (2.5 MHz) for the three IceRadar antenna sets. The 5 MHz NVE-radar antennas were also run using an in-  
220 line configuration, but with 32 m between antenna mid-points. By contrast, the shielded 450 MHz and 500 MHz  
221 Malå antennas were oriented perpendicular to the travel direction and with a 0.18 m antenna separation. To avoid  
222 interference between radar systems during data collection, the two snowmobiles travelled at a distance of more  
223 than 50 m. For frequencies of 25 MHz and above, each measurement (trace) was stacked between 4 and 8 times  
224 to increase the signal-to-noise ratio, whereas the 2.5 and 5 MHz measurements were stacked 256 times. Ice  
225 thickness measurements were collected at a constant time interval, which varied according to limitations in the



226 different radar systems. The distance between individual traces along radar profiles was affected by this and our  
 227 travel speed ( $\sim 15 \text{ km h}^{-1}$ ). Measurements collected with antenna frequencies ranging between 25 and 500 MHz  
 228 were sampled at the highest rate (trace distances of  $\sim 0.2\text{--}2 \text{ m}$ ). Therefore, while these measurements constitute  
 229 a significant proportion of total datapoints (Table 1), the vast majority of data coverage is attributed to ice thickness  
 230 observations along 5 and 2.5 MHz profiles, which were collected less densely. In general, ground-based  
 231 measurements of ice thickness were registered at intervals ranging between 3 and 6 m, while airborne  
 232 measurements were 3 to 20 m apart. GNSS locations along survey lines were recorded every 1 s with a horizontal  
 233 positioning accuracy of up to 5 m for the Malå radar system (G-Star IV BU-353S4 receiver) and 3 m for the IceRadar  
 234 system (Garmin GPSx OEM sensor). In addition, differential GNSS (DGNSS) measurements were carried out  
 235 independently of the radar measurements in some regions.

236

237 **Table 1: Survey dates and equipment used for ice thickness measurements during the 2018–2023 field campaigns. The**  
 238 **number of datapoints refers to the post-processed and interpreted dataset. Institutions are Western Norway University**  
 239 **of Applied Sciences (HVL), the Norwegian Water Resources and Energy Directorate (NVE) and University of Bergen**  
 240 **(UIB).**

Method	Radar type	Frequency	Points	Survey dates	Institutions	
<i>Ground-based radar</i>	IceRadar	2.5 MHz	15712	18–19 April 2018	HVL	
	NVE-radar	5 MHz	18569	18 April 2018	NVE	
	IceRadar Malå GPR Malå GPR	2.5 and 5 MHz 50 MHz RTA 450 MHz shielded	99745 4503 15308	11–18 April 2021	HVL	
	RadarTeam Subecho 40	40 MHz	32533	16–17 April 2021	NVE	
	IceRadar Malå GPR	2.5 MHz 25 MHz RTA	5221 5753	20–24 April 2021	UIB	
	IceRadar Malå GPR	10 MHz 50 MHz RTA	4825 2723	4 September 2021	HVL	
	IceRadar	5 MHz	11769	8 March 2022	HVL	
	IceRadar Malå GPR	5 MHz 25 and 50 MHz RTA	18424 11938	19–22 March 2022	HVL	
	IceRadar	5 MHz	5856	5–6 April 2022	NVE	
	IceRadar Malå GPR Malå GPR	5 MHz 50 MHz RTA 500 MHz shielded	53061 12509 4282	20–21 April 2022	HVL	
	IceRadar	2.5 MHz	621	22 March 2023	HVL	
	<i>Airborne radar</i>	IceRadar	5 MHz	5725	22 March 2022	UIB
		IceRadar	5 MHz	5151	7 April 2022	UIB and HVL
IceRadar		5 MHz	5267	26 April 2022	HVL	
IceRadar		5 MHz	12064	20 April 2023	HVL	

241

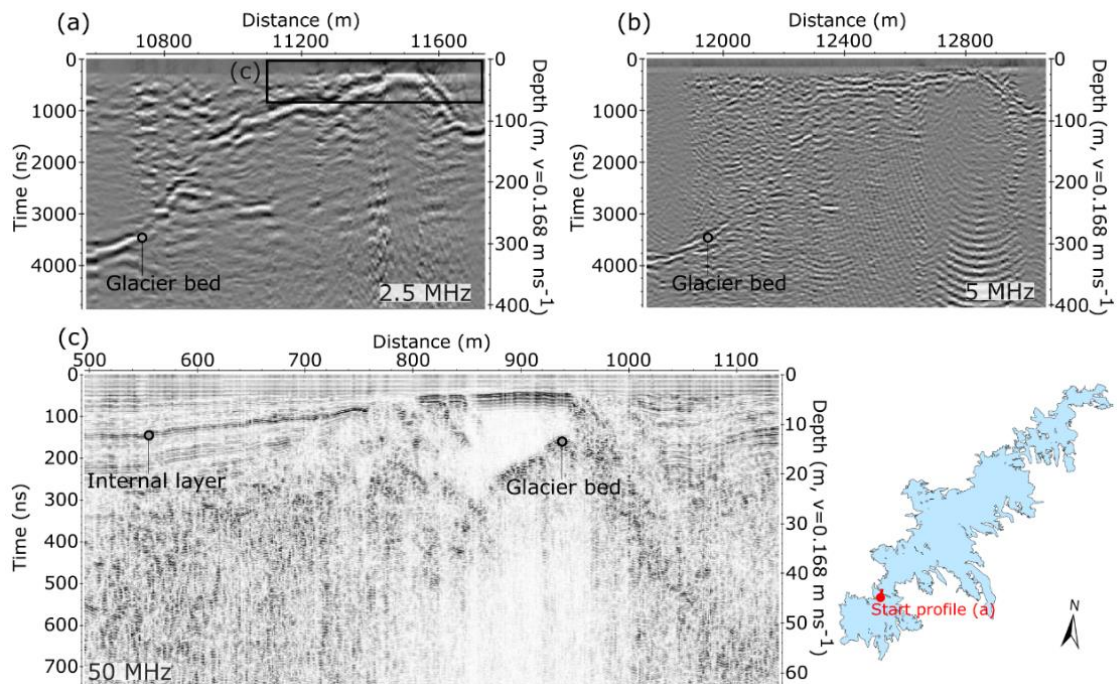
### 242 **3.2 Data processing and interpretation**

243 The raw GPR data was primarily processed using the ReflexW module for 2D data analysis (Sandmeier Scientific  
244 Software, version 8.5). Initial data processing involved adding GNSS positions for antenna midpoints to all traces,  
245 merging individual shorter profiles into larger segments, and assigning a constant trace increment along each  
246 segment to allow for subsequent migration. We chose a trace increment close to the mean value during travel to  
247 avoid deleting or introducing too many traces to the original dataset. Following the initial data sorting, we used a  
248 combination of 1) dewow, 2) Butterworth bandpass filtering, 3) time zero correction, 4) dynamic correction, 5)  
249 energy decay gain, and 6) f-k Stolt migration on all ground-based measurements. For the GPR measurements  
250 collected with 2.5 and 5 MHz systems, processing steps 3) and 4) are important to account for the influence of the  
251 large antenna separation on first signal arrival times and the radar wave path through the ice. Further filtering was  
252 required on the airborne measurements due to significant system-related noise. The processing routine for this  
253 portion of the dataset consequently involved applying an adaptive filter using the IceRadarAnalyzer processing  
254 software (Blue System Integration Ltd., version 6.3.1. beta) to remove unwanted signals from the radar profiles, in  
255 addition to dewow and bandpass filtering. Subsequent static correction was undertaken in ReflexW using manually  
256 delineated arrival times of the glacier surface reflection, after which energy decay gain and f-k Stolt migration were  
257 applied.

258

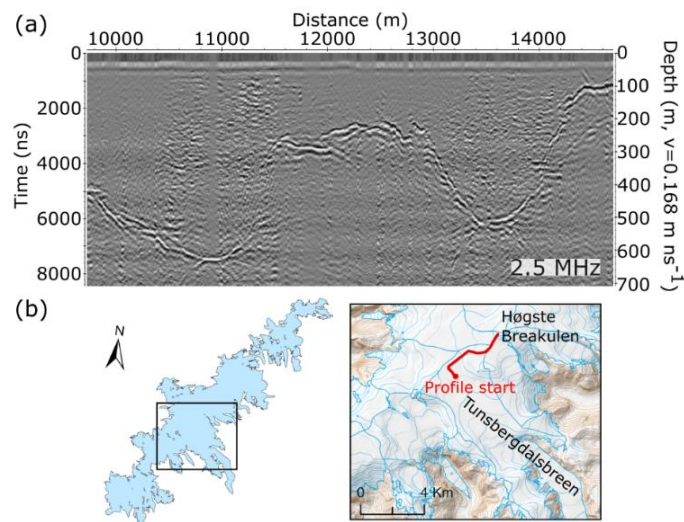
259 Following data processing, we observed a bed reflection along most 2.5 and 5 MHz radar segments and in higher  
260 frequency measurements collected in ice-marginal regions (Fig. 3). The bed reflections were delineated manually,  
261 and we calculated ice thickness from the reflection two-way travel time by assuming a constant radio-wave velocity  
262 in ice of  $0.168 \text{ m ns}^{-1}$ , similar to that used on other glaciers in Norway and abroad (Dowdeswell and Evans, 2004;  
263 Navarro and Eisen, 2009; Andreassen et al., 2012a; Yde et al., 2014; Johansson et al., 2022).

264



265  
 266 **Figure 3: Example of measurements with (a) 2.5 MHz, (b) 5 MHz and (c) 50 MHz antennas on shallow ice along a profile**  
 267 **travelling north near Grensevarden (Fig. 1). The 2.5 and 50 MHz profiles were collected along identical tracks in 2021,**  
 268 **while the 5 MHz measurements are from 2022 along a profile located ~50 m from these tracks. The radargrams illustrate**  
 269 **well the difference in resolution and penetration depth resulting from variations in antenna frequency. The lowest**  
 270 **frequency measurements provide information on bed topography along the entire profile, while the 50 MHz profile**  
 271 **allows for accurate measurements of thin ice and offers evidence of internal ice characteristics.**

272  
 273 The range of frequencies allows for a detailed mapping of both shallow and deep ice at the best possible resolution.  
 274 In shallow regions, ice thickness was most accurately determined from the highest frequency measurements, which  
 275 also provide information on snow (450 and 500 MHz data only), firn and internal layer characteristics (Fig. 3c). In  
 276 this paper, we present only the interpreted ice thickness from these higher frequency measurements. In general,  
 277 GPR measurements at Jostedalsbreen are characterised by strong scattering and rapid attenuation of the radar  
 278 signal (Fig. 3c), as is typical for radar surveys on temperate glaciers (Smith and Evans, 1972; Ogier et al., 2023).  
 279 Occasionally, regions of more transparent ice were observed in the higher frequency measurements (Fig. 3c).  
 280 These likely indicate either zones that are above the internal water table or isolated patches of cold (frozen) ice.  
 281 While the 5 MHz antennas generally performed well in depths of up to 400–500 m, the advantage of using 2.5 MHz  
 282 antennas was evident in areas with sloping bed topography (Fig. 3a and 3b) and in the deepest regions, where  
 283 reflectors were sometimes weak or absent, even with the 2.5 MHz system (Fig. 4).

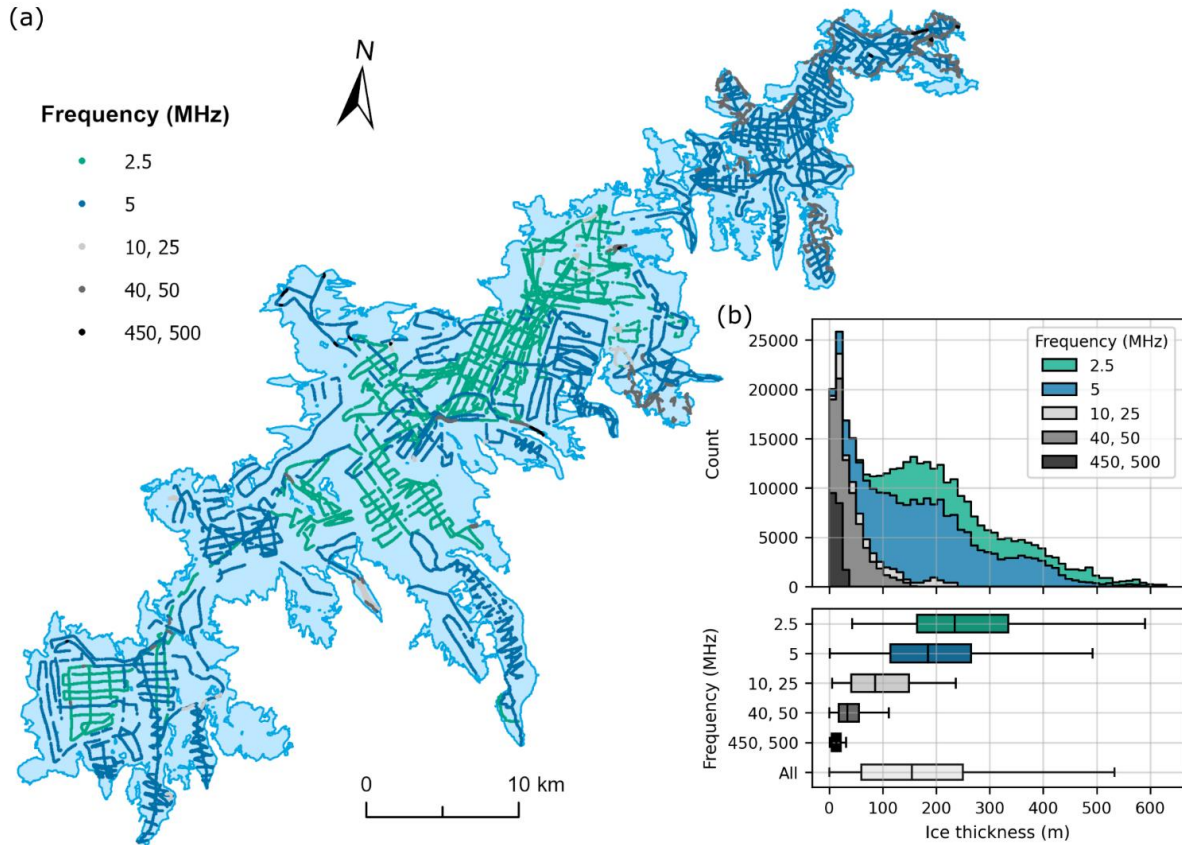


285  
 286 **Figure 4: (a) Example radargram of measurements with 2.5 MHz antennas. (b) The profile was located along a transect**  
 287 **in the upper part of Tunsbergdalsbreen (Fig. 1), where the thickest ice was observed. The detailed background map in**  
 288 **(b) is from the Norwegian Mapping Authority (WMS for Topografisk Norgeskart available at <https://www.geonorge.no/>)**  
 289 **and the 2019 outlines of glacier units on (b) are from Andreassen et al. (2022).**

290  
 291 The efficiency of snowmobile transport during the fieldwork depended strongly on the snow conditions and varied  
 292 significantly between field seasons. For example, valley access onto Tunsbergdalsbreen was possible in 2022,  
 293 when the snow cover was thick, but attempts to drive onto the glacier tongue in 2023 had to be abandoned. The  
 294 helicopter measurements generally cover regions that were inaccessible on snowmobile, either due to steep and/or  
 295 crevassed terrain, or unfavourable snow conditions. Consequently, helicopter measurements provide a valuable  
 296 addition to the ground-based measurements. However, the airborne measurements generally had a lower  
 297 penetration depth than ground-based measurements using the same antenna frequency, primarily due to increased  
 298 electronic noise and radar wave attenuation, as well as scattering of the radar signal caused by large surface  
 299 crevasses present in many airborne surveyed regions. Despite these challenges, bed reflectors were generally  
 300 observed at depths of up to 350–400 m of ice in airborne measurements (Fig. B1).

301  
 302 After the initial ice thickness calculations, all observations of ice thickness were plotted in ArcGIS Pro, where we  
 303 deleted points collected with the 5 and 2.5 MHz radar systems in sharp turns, as the long antennas were not fully  
 304 extended at these locations. Profile lines collected alongside and in close proximity to valley walls were also  
 305 removed to limit the influence of off-nadir reflections in the dataset. In marginal regions with both high- and ultra-  
 306 high frequency observations, high-frequency measurements (2.5 and 5 MHz) were deleted due to their comparably  
 307 lower accuracy. To produce a consistent dataset of ice thicknesses for the entire Jostedalbreen, we double-  
 308 checked interpretations at all locations where ice thickness observations from crossing profiles differed by more

309 than 15 m. When contrasting observations suggested that a transect was influenced by off-nadir reflectors or other  
310 uncertainties such as resolution issues, the presence of multiple reflectors or location uncertainties, these  
311 datapoints were removed from the dataset. The combination of multiple frequency measurements in many regions  
312 of the ice cap has resulted in a final dataset where both thin and very thick ice is represented in a generally  
313 satisfactory resolution (Fig. 5).  
314



315  
316 **Figure 5: (a) Ice thickness measurements across Jostedalsgreen categorized according to antenna frequency. The**  
317 **thickest regions of the ice cap were measured using the lowest frequency antennas, while higher frequencies were**  
318 **applied in the more marginal and thinner regions. (b) Histogram (top) and boxplot (bottom) of measurements of ice**  
319 **thickness categorised by antenna frequency. Boxes represent the interquartile range (IQR; the spread of the middle**  
320 **50 % of the data), with medians indicated by vertical lines. Whiskers extend to the highest and lowest values that are**  
321 **within the 1.5\*IQR limits. The analysis shows that measurements collected using higher frequency GPR systems**  
322 **dominate at low ice thickness, while 5 and 2.5 MHz GPR systems were the better choice for ice thicknesses above ~100**  
323 **m.**

### 324 **3.3 Homogenization to 2020 DTM and calculation of glacier bed topography**

325 Following the data processing and interpretation of the GPR measurements, the bed topography elevation beneath  
326 Jostedalsbreen was calculated from the point values of ice thickness and a recent 10 m national digital terrain  
327 model (DTM10) from the Norwegian Mapping Authority. This allowed for a comparison with previous observations  
328 of glacier bed elevations (see section 4.2). For Jostedalsbreen, the DTM10 is derived from airborne laser scanning  
329 (lidar) collected by Terratec over a seven-day period in August 2020, that covered Jostedalsbreen and surrounding  
330 area with a point density of minimum 2 pp m<sup>-2</sup> (Terratec, 2020). The central part of the ice cap was scanned on 9  
331 August, the western part on 10 August and the eastern part on 15 August. The accuracy of the final point cloud is  
332 assumed to be ±0.1 m (Andreassen et al., 2023). The 2020 survey (2020 DTM) covers the entire Jostedalsbreen,  
333 except for the lower tongue of Tunsbergdalsbreen (Andreassen et al., 2023) where surface elevation data in DTM10  
334 is derived from stereophotogrammetry using 2017 orthophotos.

335  
336 To prevent discontinuities in the ice thickness dataset and elevation of bed topography, all ice thickness  
337 measurements were homogenised to correspond to the date of the 2020 DTM. We used DGNS observations of  
338 surface elevation to calculate an area dependent mean surface elevation difference between the time of acquisition  
339 of GPR data and the 2020 DTM. Calculations show that DGNS measurements exceed the 2020 DTM by average  
340 values ranging from 0.6 m (northern parts in spring 2022) to 3.9 m (central parts in spring 2018), reflecting surface  
341 changes such as the increased depth of the snowpack during spring measurements compared to the end of  
342 summer lidar scan. The elevation of the bed topography was calculated by subtracting the homogenised ice  
343 thicknesses from the DTM10.

### 344 **3.4 Ice thickness measurement uncertainties**

345 The multifrequency dataset of crossing profiles allows for an investigation of discrepancies between measurements  
346 with various degrees of vertical resolution as a means to evaluate ice thickness uncertainties. Here, we present the  
347 results of a comparison of ice thicknesses at intersection points (crossover analysis), in addition to the total  
348 calculated measurement uncertainty for each datapoint following the method described by Lapazaran et al. (2016).  
349 In the final dataset, profiles crossed at 1207 locations (not counting profiles collected along identical tracks). Ice  
350 thicknesses in crossing points had a mean absolute difference (MD) of 6.8 m with a standard deviation (SD) of 5.8  
351 m, which when expressed in relation to ice thickness equals a MD of 5.0 % (7.1 % SD). Not surprisingly, the  
352 discrepancy between values increased with decreasing frequency and hence vertical and horizontal resolution.  
353 The largest discrepancies were observed where at least one of the crossing profiles was collected with 2.5 MHz  
354 antennas (MD of 8.4 m and a 6.7 m SD; maximum discrepancy of 39 m; n=538), whereas profiles collected with  
355 500 and 450 MHz antennas generally corresponded better with other observations (MD of 3.7 m and a 3.1 m SD;

356 maximum discrepancy of 10 m; n=23). The crossover analysis also facilitated an assessment of the performance  
357 of the lowest frequency measurements when compared to higher resolution and more accurate ice thickness  
358 observations collected using antenna frequencies of 25–500 MHz. The comparison show that ice thicknesses  
359 measured with 2.5 and 5 MHz antennas were generally (but not always) somewhat larger than those measured  
360 with higher frequency antennas. The ice thicknesses measured with 2.5 and 5 MHz antennas were on average 8.0  
361 m (6.9 m SD; n=31) and 3.6 m (4.8 m SD; n=136) greater, respectively, than those measured with the 25–500 MHz  
362 antennas. It is unclear exactly why these differences occur. Although a systematic bias is unfortunate, the observed  
363 differences are well below the vertical resolution (evaluated conservatively as  $\frac{1}{2}$  wavelength,  $\lambda$ ) of both the 2.5 MHz  
364 (33.6 m) and 5 MHz (16.8 m) antennas, as well as the total calculated measurement uncertainty described below.

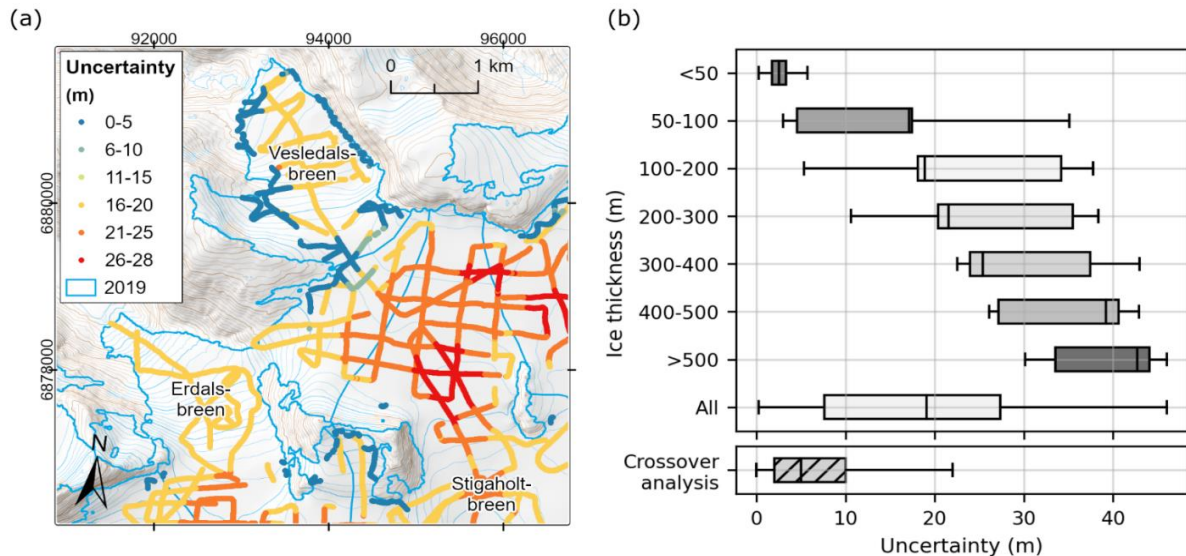
365  
366 To evaluate the performance of the 5 MHz helicopter system, we compared discrepancies between ice thicknesses  
367 measured at intersecting airborne and ground-based profiles. We found an MD of 7.2 m (4.6 m SD; n=56) between  
368 airborne and ground-based ice thickness measurements, which is comparable to values found for all ground-based  
369 and crossing 5 MHz profiles (MD of 6.5 m and a 5.0 m SD; n=705). It is worth noting that helicopter measurements  
370 along several outlet glaciers and at steep ice falls were conducted along centreline profiles, where off-nadir  
371 reflectors may affect the results (Fig. 1c). This could result in an underestimation of ice thickness in these regions.  
372 Where measurements along cross profiles suggested that the centreline values were unreliable, the latter were  
373 removed from the dataset. However, in most cases centreline values compared well with measurements along  
374 cross profiles and were largely included in the dataset.

375  
376 As a crossover analysis does not encompass all potential uncertainties associated with ice thickness  
377 measurements, it is generally considered to only provide a rough approximation of uncertainty (Lapazaran et al.,  
378 2016). Consequently, we calculated the total measurement uncertainty for each ice thickness observation using  
379 the method described by Lapazaran et al. (2016), which is based on the root-sum-of-squares of both uncertainties  
380 in the ice thickness measurements and the measurement position. Using this approach, we included uncertainties  
381 related to the radio-wave velocity, which we assumed to be 5 %, as recommended by Lapazaran et al. (2016) when  
382 the same velocity is applied in both accumulation and ablation areas. In addition, our uncertainty calculations  
383 considered the signal resolution ( $\lambda/2$ ) and positioning uncertainty. The latter was accounted for by calculating the  
384 largest measured ice thickness difference within a circle, with the radius determined by the respective GNSS  
385 uncertainty. Using this approach, total ice thickness uncertainties were primarily controlled by antenna frequency  
386 and ice thickness because of their influences on vertical resolution and the uncertainty caused by the constant  
387 radio-wave velocity, respectively (Fig. 6 and Fig. C1).

388

389 The calculated combined uncertainties of the ice thickness measurements amounted to an average of 19.6 m for  
 390 the entire dataset (SD of 12.1 m;  $n = 351\,559$ ), while mean ice thickness uncertainties ranged between 36.5 m (SD  
 391 of 2.5 m) and 20.2 m (SD of 3.1 m) for 2.5 and 5 MHz measurements, respectively, and 1 m (SD of 0.5 m) for 450  
 392 and 500 MHz measurements. The large mean uncertainty estimate calculated for most ice thickness observations  
 393 was primarily a result of the conservative treatment of signal resolution and the assumed 5 % uncertainty from  
 394 applying a single radio-wave velocity value to the entire ice cap despite ice cap-wide variations in snow, firn, and  
 395 thermal ice conditions. The significantly larger measurement uncertainty found using the method of Lapazaran et  
 396 al. (2016) compared to the crossover analysis (Fig. 6b), implies that the former approach leads to an overestimation  
 397 of uncertainties associated with relatively low frequency (below  $\sim 10$  MHz) ice thickness measurements, particularly  
 398 in regions with thick ice. We therefore suggest that the crossover analysis and the calculated measurement  
 399 uncertainty represent a lower and upper estimate, respectively, of the uncertainties associated with each ice  
 400 thickness observation. In the datafile compilation presented here, we include only the upper estimate of total  
 401 measurement uncertainty.

402



403

404 **Figure 6: (a) Calculated ice thickness measurement uncertainties at Vesledalsbreen (Fig. 1) and surrounding glaciers.**  
 405 **Variations in measurement uncertainties are primarily controlled by antenna frequency, with <5 m uncertainty for 500**  
 406 **MHz measurements, between 6 and 13 m uncertainty for 50 MHz measurements and  $\geq 14$  m for 5 MHz measurements.**  
 407 **The largest measurement uncertainties are found in regions with thick ice, illustrating the influence of ice thickness**  
 408 **on the uncertainty calculations. (b) Distribution of calculated absolute uncertainty in ice thickness by thickness class**  
 409 **and for all measurements following the method described by Lapazaran et al. (2016), as well as that observed in the**  
 410 **crossover analysis. Boxes represent the interquartile range (IQR; the spread of the middle 50 % of the data), with**  
 411 **medians indicated by vertical lines. Whiskers extend to the highest and lowest values that are within the 1.5\*IQR**  
 412 **limits. The background map in (a) is from the Norwegian Mapping Authority (WMS for Topografisk Norgeskart available at**  
 413 **<https://www.geonorge.no/>) and the 2019 outlines of glacier units are from Andreassen et al. (2022). The coordinate**  
 414 **system is UTM 33N, datum ETRS\_1989.**



415 **3.5 Description of datafile compilation**

416 The ice thickness point values from Jostedalsbreen were compiled in a format similar to that of the Glacier  
 417 Thickness Database (GlaThiDa Consortium, 2020; Welty et al., 2020) for straight-forward application in future  
 418 studies. Data were stored in a CSV (comma-separated values) file with attributes describing the data (Table 2),  
 419 and a DOI is provided for the ice thickness dataset. Consequently, the dataset follows the FAIR principles of  
 420 optimised findability, accessibility, interoperability, and reusability.

421

422 **Table 2: Attributes used in the point dataset of ice thickness values on Jostedalsbreen.**

Attributed field	Unit	Description
SURVEY_DATE	YYYYMMDD	Survey date
PROFILE_ID	Text	Identifier of processed radar profile
POINT_ID	Number: 1-n	Point identifier
ANTENNA_FREQUENCY	MHz	Antenna frequency of measurement
SURVEY_METHOD	Text: H, S or F	Means of transport during survey (H: Helicopter, S: Snowmobile, F: Foot)
GNSS_SOURCE	Number: 0 or 1	Position information (0: Radar GNSS (lowest uncertainty) and 1: External GNSS source or some degree of interpolation across minor data gaps)
POINT_LAT	DDD.DDDDDD°	Latitude of point value
POINT_LON	DDD.DDDDDD°	Longitude of point values
GNSS_ELEVATION	m a.s.l.	Surface elevation from GPR GNSS
THICKNESS	Meter	Ice thickness value
THICKNESS_UNCERTAINTY	Meter	Uncertainty in ice thickness based on Lapazaran et al. (2016)
THICKNESS_2020DTM	Meter	Ice thickness value homogenised to the 2020 DTM surface*. Corrected for differences in surface elevation during survey years relative to the 2020 DTM.

423 \*Survey date August 2020 except for the lower part of Tunsbergdalsbreen.

424

425 Most of the attributes in the table containing ice thickness point values are self-explanatory and identical to those  
 426 in GlaThiDa. However, data entries such as SURVEY\_METHOD, GNSS\_SOURCE and THICKNESS\_2020DTM  
 427 are additional attributes to describe the Jostedalsbreen data collection. In addition to the datafile containing the  
 428 complete ice thickness dataset (n = 351 559 entries), we provide a thinned-out version of this dataset (n = 35 100  
 429 entries) consisting of point values extracted randomly from the full dataset but with a minimum distance of 20 m.  
 430 The smaller dataset allows for easier plotting and analysis.

### 431 **3.6 Model-based ice thickness inter- and extrapolation**

432 While the dense network of GPR profiles across large parts of the ice cap provides direct local information on ice  
433 thickness on 59 out of the 81 glacier units that make up Jostedalbreen ice cap (Fig. 1), an extrapolation to  
434 unmeasured regions was necessary to produce grids of ice thickness and bed topography which cover the entire  
435 Jostedalbreen. Here, we apply an approach that combines the advantages of inter- and extrapolation of point ice  
436 thickness observations with those of ice thickness modelling from an inversion of surface topography (Huss and  
437 Farinotti, 2014; Grab et al., 2021). The basis of this approach is an ice thickness model originally developed for  
438 global-scale applications (Huss and Farinotti, 2012). The model was used in the Ice Thickness Model  
439 Intercomparison eXperiment (ITMIX and ITMIX2, Farinotti et al., 2017, 2021) and performed well in estimations of  
440 ice thickness distribution and bed topography in comparison to a wide range of other approaches. This was the  
441 case both if no nearby ice thickness measurements were available, and when such observations were integrated  
442 for constraining model parameters.

443  
444 The general concept of the model for glaciers without measurements is to derive local ice thickness from surface  
445 characteristics. The model relies on glacier surface hypsometry of all individual glacier units of Jostedalbreen,  
446 discretised into 10 m elevation bands. Variations in the valley shape and the basal shear stress along each outlet  
447 glacier's longitudinal profile, as well as an estimated constant basal sliding fraction of 0.5 (e.g., Huss and Farinotti,  
448 2012), are taken into account. Ice volume fluxes are computed along a longitudinal profile based on calibrated  
449 mass balance gradients. Subsequently, ice thickness is calculated by inverting the flow law for ice (Glen, 1955),  
450 thus assuming parallel flow consistent with the shallow-ice approximation. Resulting averages of elevation-band  
451 ice thickness are then interpolated to a regular grid by considering both local surface slope and distance from the  
452 glacier margin, excluding ice divides (for details see Huss and Farinotti, 2012). For glacier units with ice thickness  
453 measurements (i.e., the vast majority of Jostedalbreen) the modelled ice thickness is first optimised to fit the  
454 measurements and then only used in unmeasured regions along with all measured point ice thicknesses in an  
455 inverse-distance interpolation scheme (see details below). Our approach provides a spatially complete ice  
456 thickness and bedrock grid that agrees with all thickness observations. We decided to use this methodology rather  
457 than approaches based on assimilating the ice flux divergence (e.g., Fürst et al., 2017; Morlighem et al., 2017), as  
458 we attribute the highest weight to fitting the comprehensive set of measurements that are at the core of the present  
459 study.

460  
461 Before initialising the model-based ice thickness inter- and extrapolation, we harmonised the spacing of the  
462 acquired profiles by taking the average of all homogenised ice thickness point data contained within the same 10  
463 x 10 m cell of the DTM10. The ice thickness point dataset and the outline of Jostedalbreen both serve as important

464 input when computing spatially distributed ice thickness. As glacier outline, we used the national glacier inventory  
465 which relies on Sentinel-2 images taken on 27 August 2019 (Andreassen et al., 2022). In this dataset,  
466 Jostedalsbreen is divided into glacier units from topographic observations on ice divides. The inventory was derived  
467 using a standard semi-automatic method and checked against orthophotos and Sentinel composites from 2017  
468 and 2019, respectively, with manual edits to correct for areas in shadow, with debris-cover, and lake outlines. The  
469 uncertainty in the outlines of the final product was estimated to be within half a pixel ( $\pm 5$  m).

470

471 Our dataset of distributed ice thickness for all Jostedalsbreen was produced by optimising modelled ice thickness  
472 to local ice thickness observations for each individual glacier unit, following a three-step procedure that consisted  
473 of (i) model optimisation, (ii) spatial bias-correction of modelled thicknesses, and (iii) spatial inter- and extrapolation  
474 relying on point values of thickness and bias-corrected model results for regions that are not covered by GPR  
475 surveys.

476

477 In step (i), we optimised the apparent mass-balance gradient (Farinotti et al., 2009) for the ablation and  
478 accumulation area, assuming a constant ratio of 1.8 between the gradients, in an automatic procedure to minimise  
479 the average misfit between modelled ice thickness and the available observations for each of the 59 outlet glaciers  
480 with ice thickness measurements. To close the mass budget, we prescribed a balanced mass budget for the entire  
481 glacier unit (see Farinotti et al., 2009). The resulting apparent mass balance distribution was then used to compute  
482 ice volume fluxes from the top to the bottom of each glacier unit, and to infer modelled ice thickness distribution.

483

484 In step (ii), the modelled ice thickness distribution from step (i) was bias-corrected using ice thickness point values.  
485 First, relative differences between modelled and measured point ice thickness distributions were evaluated. These  
486 differences were then spatially inter- and extrapolated based on an inverse-distance weighting scheme that results  
487 in a smooth field over the entire Jostedalsbreen and allows extracting large-scale spatial variations in misfits. This  
488 relative spatial ice thickness correction field was then superimposed on the modelled ice thickness distribution,  
489 resulting in a bias-corrected model-based ice thickness distribution that accounts for the differences between  
490 observed and modelled ice thickness at a spatially distributed scale.

491

492 In the final step (iii), we spatially interpolated the ice thickness distribution based on (1) all available ice thickness  
493 observations, (2) the model results adjusted in steps (i) and (ii) in regions that were not covered by direct  
494 measurements (buffered in a distance of 100–200 m around available observations depending on outlet glacier  
495 size), and (3) the condition of zero ice thickness on the glacier margin, except for ice divides. The combined dataset  
496 of measured and modelled point ice thickness was directly interpolated using an inverse-distance weighting  
497 scheme to achieve a full coverage for each glacier unit at a 10 m grid spacing.

498

499 The ice thickness at ice divides was obtained from interpolated results for neighbouring glacier units, and then also  
500 entered the interpolation. Estimates for ice thickness at ice divides is, thus, given by nearby direct measurements  
501 or model results. Furthermore, for a few situations with poorly constrained ice divide thicknesses a set of individually  
502 estimated point thicknesses was included to increase the robustness of spatially complete ice thickness and  
503 bedrock grid. These estimated point ice thicknesses were acquired from a direct interpolation of nearby GPR  
504 profiles in ArcGIS pro, that involved (1) a 20 m grid spline interpolation (8 sector search radius) of ice thickness  
505 measurements and subsequent extraction of 10 m ice thickness contour lines, (2) smoothing of contour lines (50  
506 m smoothing tolerance), and (3) a Topo to Raster interpolation from smoothed contour lines. Repeating the  
507 complete procedure several times ensured convergence and thus consistency of thicknesses on both sides of the  
508 ice divides, thus avoiding thickness steps at ice divides even though glacier units were treated separately in our  
509 approach. For glacier units without GPR measurements, the ice thickness model was run using average calibrated  
510 parameters of the apparent mass-balance gradient from all outlet glaciers with direct observations. This direct  
511 modelling of ice thickness, however, was only relevant for small and mostly thin glacier units within Jostedalsgreen,  
512 and account for just 1.9 % of the total inferred volume of the ice cap. We finally combined all resulting ice  
513 thicknesses from the 81 glacier units contained in Jostedalsgreen into a complete coverage with a spatial resolution  
514 of 10 x 10 m.

### 515 **3.7 Bed topography and potential future lakes**

516 Bed topography was obtained by subtracting distributed ice thickness from the DTM10 ice surface elevation. The  
517 resulting grid of bed topography was then smoothed with a spatial filter of 20–50 m (depending on glacier basin  
518 area) to remove remaining discontinuities at ice divides, as well as unrealistic small-scale variability in calculated  
519 bed topography that cannot be inferred with the applied methodology and will originate from surface features.  
520 Depressions in the bed topography might act as potential future lakes after complete disappearance of the ice  
521 cover. Even though the uncertainty in detecting the extent and volume of such depressions is large, we derived a  
522 map of potential lake area and depth from the map of subglacial bed topography. This was achieved by using a  
523 sink fill algorithm that detected depressions, after which the depth and volume of each depression was determined  
524 by artificially filling the depression until they overflow. This resulted in an inventory of individual potential glacier  
525 lakes, including the relevant attributes, such as elevation, area, volume, or maximum depth.

### 526 **3.8 Uncertainties in inter- and extrapolated ice thickness**

527 The uncertainty in inter- and extrapolated ice thickness is composed of two elements: (1) the uncertainty in  
528 measured ice thickness, and (2) the uncertainty induced when extrapolating point ice thickness across the entire  
529 ice cap supported by the model-based approach. These two elements of uncertainty are estimated with separate  
530 experiments, and are then propagated through the methodology described above to derive a spatially distributed  
531 uncertainty map for the entire ice cap.

532  
533 As described in section 3.4, the uncertainty associated with each point value of ice thickness was calculated  
534 following Laparazan et al. (2016). We conservatively assume all uncertainties across the entire ice cap to be  
535 correlated and generate a dataset with maximum and minimum observed ice thickness according to the above  
536 uncertainties. Based on these two datasets, we repeated the complete approach described in section 3.6 using  
537 each of these datasets. Two additional experiments were conducted to assess the uncertainty caused by  
538 extrapolating observations to unmeasured regions. Relevant parameters of the ice thickness model were set to the  
539 maximum or the minimum of conservative, but physically meaningful, ranges. This was performed for (1) the  
540 viscosity of ice, (2) the assumed fraction of basal sliding, and (3) the apparent mass balance gradients. In both  
541 experiments, the reference dataset of point ice thickness values was used for calibration (see Section 3.6), such  
542 that the resulting thickness grids differ mostly in regions where ice thickness is solely inferred by the model.

543  
544 Finally, we combined the offset from the reference ice thickness at all grid cells for the four experiments described  
545 above (two for measurement uncertainty, two for model uncertainty) based on the root-sum-of-squares. This results  
546 in an absolute and a relative uncertainty grid. Local uncertainties were bounded to not exceed the grid cell's  
547 reference ice thickness which occurred in a few instances close to glacier margins. To assess the relevance of  
548 additionally set thickness points along ice divides used to better constrain the thickness inter- and extrapolation in  
549 these regions (see Section 3.6.) we performed an experiment where these supporting points were removed. We  
550 find that the effect on the inferred total ice volume of Jostedalsbreen is minimal (-1.1%), and that local thicknesses  
551 are affected by 1.2 m on average (median absolute difference).

552  
553 We note that beyond the uncertainties estimated above, our dataset of gridded thickness and bedrock for entire  
554 Jostedalsbreen comes with some limitations that should be considered regarding the usage: We intentionally rely  
555 on a statistical inter- and extrapolation of measured point thickness here and supplement this data with results from  
556 modelling in unmeasured regions. This might result in inconsistencies with the application of a three-dimensional  
557 ice flow model as our product is not optimised to correspond to a smooth flux-divergence field. Nevertheless, we  
558 argue that in the frame of the present publication, whose main emphasis is on measured ice thickness, we strive

559 to optimally make use of these observations and to attribute them with the highest weight in our gridded dataset.  
560 This also drives the decision to post our results on a 10 m grid, which may imply an exaggerated accuracy for  
561 regions without direct measurements but allows resampling to coarser resolutions, depending on the specific  
562 application.  
563

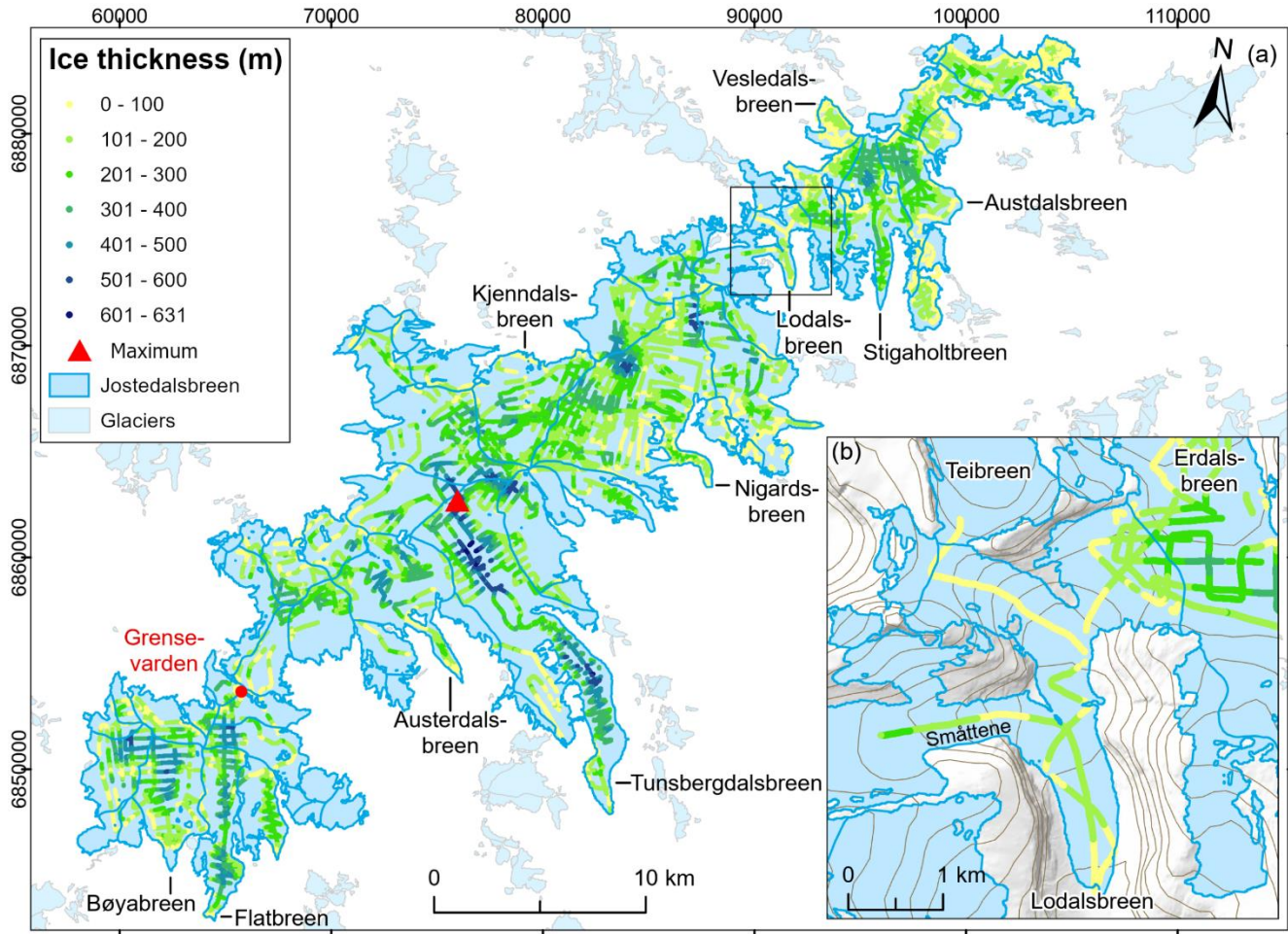
## 564 **4 Results**

### 565 **4.1 Measurements of ice thickness**

566 The dataset presented here provides ice thickness point values for 59 of the 81 glacier units that constitute the  
567 Jostedalbreen 2019 inventory. These 59 glaciers cover 437 km<sup>2</sup>, or 95 % of the total area of the ice cap (458 km<sup>2</sup>  
568 in 2019). All parts of Jostedalbreen are now less than 900 m from a point of known ice thickness (measurement  
569 or glacier outline), while distances to a known point are less than 300 m for 90 % of the ice cap and less than 100  
570 m for 49 % of the ice cap. A maximum ice thickness of 631 m (or 628 m when referring to 2020 DTM) was measured  
571 in the upper accumulation area of Tunsbergdalsbreen, which is the largest outlet glacier of Jostedalbreen and  
572 located in the central part of the ice cap (Fig. 4 and 7). In Jostedalbreen South and North, ice thickness reaches  
573 maximum values of ~520 and ~430 m, respectively. In general, the thickest ice at Jostedalbreen is found in the  
574 flattest areas of the ice cap, while thinner ice of less than 100 m thickness covers protruding hills. In the northern  
575 parts, the highest mountains in the landscape surrounding Stigaholtbreen (Fig. 6a and 7) are already partially ice-  
576 free, giving the ice cap a more disjointed appearance in this region.

577  
578 Along the south-eastern margin of Jostedalbreen, large outlet glaciers flow far into the valleys below. Particularly  
579 thick ice is found along the three glacier tongues of Tunsbergdalsbreen (up to ~615 m), Flatbreen (up to ~435 m)  
580 and Stigaholtbreen (up to ~320 m) (Fig. 7). These outlet glaciers are characterised by large accumulation areas  
581 from which ice flows relatively unrestricted from the innermost parts of the ice cap plateau and along deep glacier-  
582 carved valleys. In comparison, thinner ice is observed along outlet glaciers where ice flows from the ice cap plateau  
583 through steep ice falls. Austerdalsbreen with its two steep ice falls and low-sloping glacier tongue, represents one  
584 such example. Here, helicopter measurements along the centre flowline of the largest of the two narrow ice falls  
585 suggest that the ice is only 40–50 m thick in the steepest parts. Below the ice falls, ice thickness reaches a  
586 maximum of ~235 m. At Nigardsbreen, ice also thins to 40–50 m as it flows through the two smallest western ice  
587 falls. Here, the main flow of ice from the ice cap plateau appears to occur through the much larger northern tributary,  
588 where centre-line ice thicknesses of more than 100 m were measured in the thinnest regions. Below the three ice  
589 falls, ice thickness reaches a maximum of ~265 m before thinning towards the famous glacier front of Nigardsbreen.

590



593

594 **Figure 7: (a) Combined ice thickness observations at Jostedalsglacier from field campaigns in 2018, 2021, 2022 and**  
 595 **2023. The point of maximum thickness is marked with a red triangle. (b) Section of Lodalsbreen with 100 m surface**  
 596 **contours. Note that the helicopter measurements along Lodalsbreen were collected during the first test flight of the**  
 597 **airborne radar system, where profile locations were positioned less than ideal in relation to the valley orientation. The**  
 598 **background mountain shadow and 100 m contour lines in (b) are from the Norwegian Mapping Authority (WMS for**  
 599 **Topografisk Norgeskart available at <https://www.geonorge.no/>). The 2019 outlines of glacier units are from**  
 600 **Andreassen et al. (2022), and the coordinate system is UTM 33N, datum ETRS\_1989.**

601

602 From the extensive measurements of ice thickness, we have identified two regions that may be particularly  
 603 vulnerable to future climate-forced changes and that have the potential to separate Jostedalsglacier into three  
 604 unconnected ice caps, North, Central, and South (Fig. 1). In the north, Lodalsbreen currently connects the  
 605 northernmost part of Jostedalsglacier with its more southern regions through three steep tributaries (Fig. 7b).  
 606 Helicopter measurements along the centre flowlines reveal that the ice thins to 50 m or less as it flows southwards

607 and into the incised valley below. Ice flowing from the western tributary is thicker, with ice thicknesses ranging  
608 between 50 and 70 m along its thinnest sections. A study of surface elevation changes at Jostedalsbreen between  
609 1966 and 2020 shows that the ice cap has experienced significant thinning in this region (Andreassen et al., 2023).  
610 This trend is likely to continue as Jostedalsbreen adjusts to warmer air temperatures. Further south on  
611 Jostedalsbreen, thin ice of less than 25 m covers the narrow stretch at Gensevarden that joins the southern part  
612 of the ice cap with its central regions (Figs. 3 and 7). Bedrock has already started protruding through the thinning  
613 ice, and the emerging rocks are likely to further accelerate the changes occurring in this part of Jostedalsbreen due  
614 to positive feedback on melting from a decreasing albedo of the surroundings. However, it is important to note that  
615 while thin ice may indicate increased vulnerability to future warming, other factors such as ice velocity and surface  
616 mass balance are important influences when considering future changes in areas with thin ice. Such considerations  
617 require ice cap-wide modelling of glacier evolution and are beyond the scope of this paper.

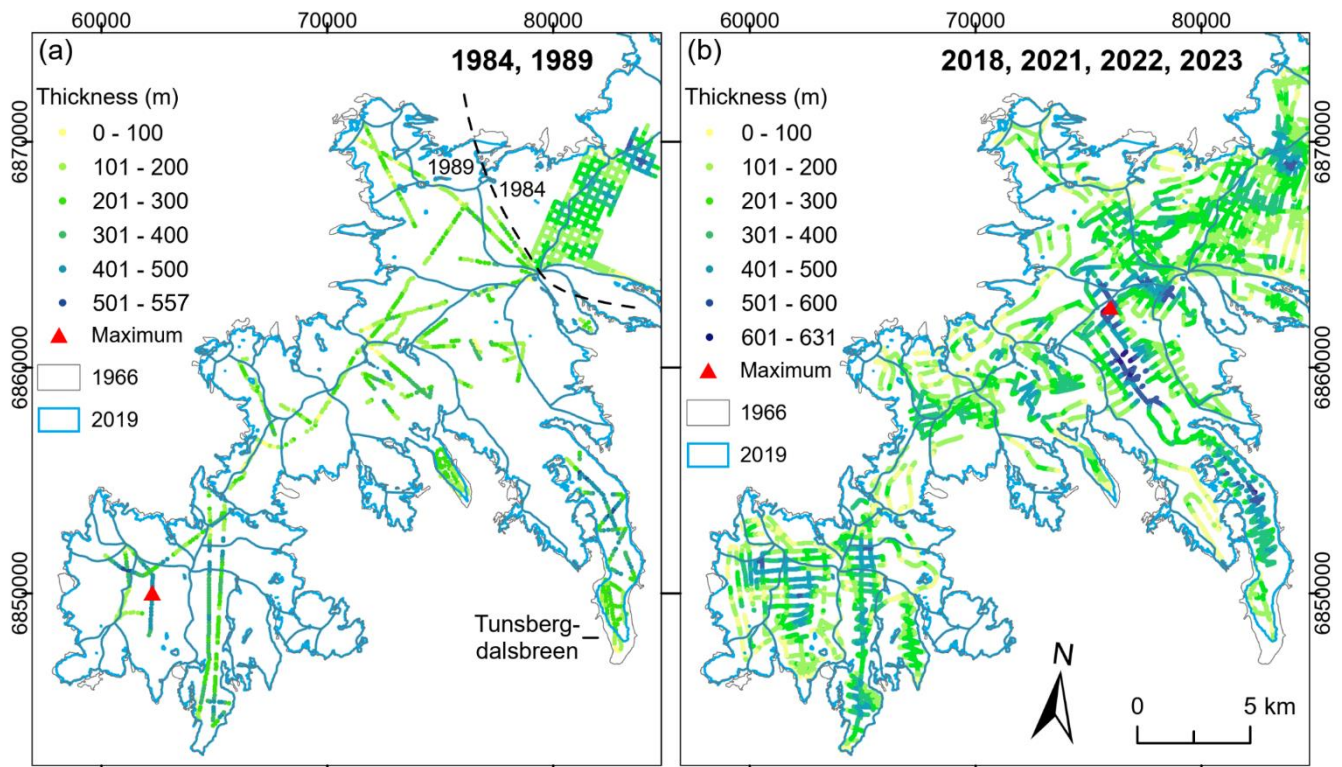
#### 618 **4.2 Comparison to previous ice thickness measurements at Jostedalsbreen**

619 The new comprehensive dataset of Jostedalsbreen ice thicknesses represents a significant improvement to  
620 previous measurements, both in relation to data quality and spatial coverage across the ice cap. We now have a  
621 much better understanding of ice thickness variations in the region and have also extended the maximum measured  
622 ice thickness from 600 m measured during the 1980s field campaigns (Sætrang and Wold, 1986) to the 631 m  
623 measured in 2021. Although the general ice thickness variability identified in the new measurements are also  
624 recognisable in the older datasets, distinct differences between the datasets are observed across the ice cap (Fig.  
625 8). Regions with thick ice are particularly poorly resolved in the earlier measurements, most likely due to limitations  
626 in the radar system applied during these field campaigns. While we believe that most of the discrepancies can be  
627 attributed to measurement uncertainties, evidence of glacier retreat since the measurements in 1989 is discernible  
628 in marginal regions.

629

630





631  
 632 **Figure 8: (a) Previous ice thickness measurements collected in the southern part of Jostedalsgleibreen in 1984 and 1989.**  
 633 **Only the 1989 dataset is included in GlaThiDa (GlaThiDa consortium, 2020). (b) Ice thickness measurements collected**  
 634 **during the 2018, 2021, 2022 and 2023 field seasons. Locations of maximum measured ice thickness during the**  
 635 **respective field campaigns are marked on both figures. The 1966 outline of Jostedalsgleibreen is from Paul et al. (2011)**  
 636 **and the 2019 outlines of glacier units are from Andreassen et al. (2022). The coordinate system on both figures is UTM**  
 637 **33N, datum ETRS\_1989.**

638  
 639 Many of the previous ice thickness measurements conducted on Jostedalsgleibreen have considerable uncertainties  
 640 in measurement positioning and surface topography. Therefore, we limit a further comparison of our measurements  
 641 to ice thickness observations on Austdalsgleibreen in the late 1980s, which we consider to be afflicted with the lowest  
 642 uncertainties (Fig. A1b). This older dataset was collected to evaluate future changes to Austdalsgleibreen due to  
 643 enhanced calving after the regulation of the proglacial lakes Austdalsgleibvatnet and Styggevatnet for hydropower  
 644 production (Hooke et al., 1989; Laumann and Wold, 1992). Ice thickness was measured in nine hot water drilled  
 645 boreholes and by GPR within an area of 600 by 1000 m, where the ice thicknesses ranged between 100 and 230  
 646 m (Fig. A1b, Sætrang and Holmqvist, 1987; Sætrang, 1988). The boreholes were drilled in September 1986 and  
 647 October 1987, while the GPR measurements used for the assessment of uncertainties were collected in April–May  
 648 1988 using an 8 MHz radar system. Comparisons between radar measurements and boreholes at the time, showed  
 649 borehole bedrock elevations between 14 m below and 1 m above radar bed elevations. The overall uncertainty of

650 the radar bed elevations was estimated to be within 7 m based on results from a radar crossover analysis and  
651 observed uncertainties in positioning and surface elevation (Sætrang, 1988).

652

653 Two radar profiles from 2022 intersected the area also mapped by GPR in 1988. To allow for a comparison with  
654 the new ice thickness measurements, we interpolated a 5 x 5 m bed elevation grid from the 1988 GPR  
655 measurements and extracted the bed elevations at the nine boreholes and 454 locations covered by the GPR  
656 survey in 2022. On average, bed elevations measured in boreholes were 4 m lower than the interpolated grid, and  
657 the grid consequently shows a good replication of variations observed in both of the two older datasets. When  
658 comparing values from the interpolated grid and those obtained in 2022, we find that bed elevations calculated  
659 from measurements in 2022 were on average 14 m lower than those found with GPR in 1988 (i.e., 2022 ice was  
660 thicker than expected from the 1988 dataset). However, it is unclear whether this discrepancy relates to  
661 uncertainties concerning the earlier or the new measurements. In this region the 2022 measurements have a  
662 measurement uncertainty of 17–20 m (Fig. C1), and the observed discrepancies are consequently within the range  
663 of combined uncertainties.

#### 664 **4.3 Distributed ice thickness, bed topography and potential future lakes**

665 The maps of ice thickness and bed topography (Fig. 9) allow for a coherent description of the variations in the  
666 morphology of Jostedalsbreen, also in regions that are not covered by GPR measurements. The two grids illustrate  
667 that thickest ice is found predominantly away from ice divides and in the prominent subglacial valleys of the largest  
668 outlet glaciers. By contrast, thinner ice and elevated subglacial bed topography are often associated with regions  
669 of the ice cap with high surface elevations. From the modelled ice thickness grid, we calculate a present (~2020)  
670 ice cap-wide mean ice thickness of 154 m  $\pm$ 22 m and an ice volume of 70.6  $\pm$ 10.2 km<sup>3</sup> (Table 3).

671

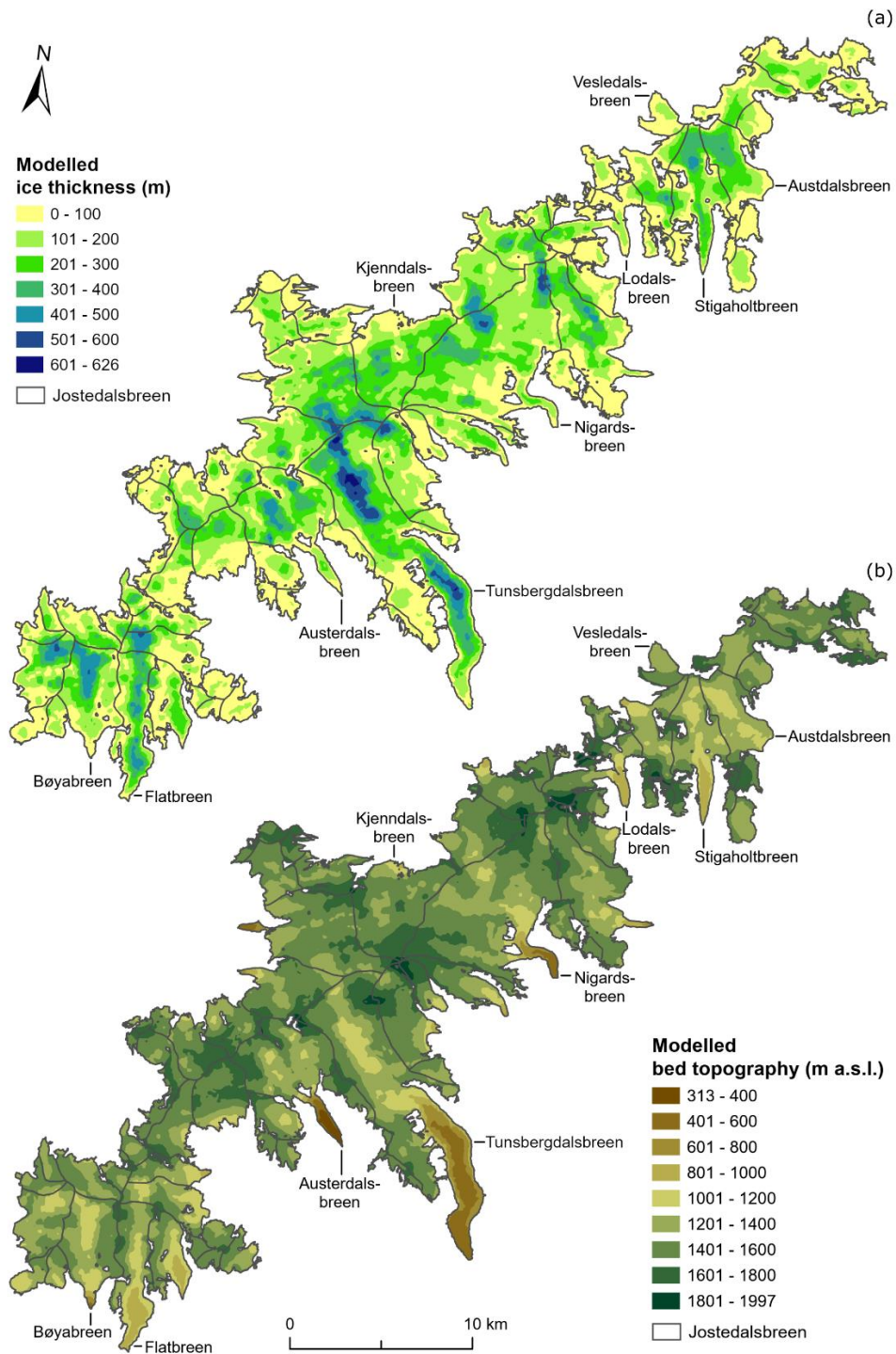
672 Absolute and relative uncertainty grids for the distributed ice thickness (Fig. 10) indicate that uncertainties in  
673 modelled ice thickness are typically small close to the GPR profiles and larger in regions where the result is based  
674 on ice thickness modelling. Overall, we find a mean uncertainty in local ice thickness of 36 m (30 %), where regions  
675 with thick ice are characterised by high absolute but low relative thickness uncertainties, and vice versa for regions  
676 with thin ice (Fig. 10).

677

678

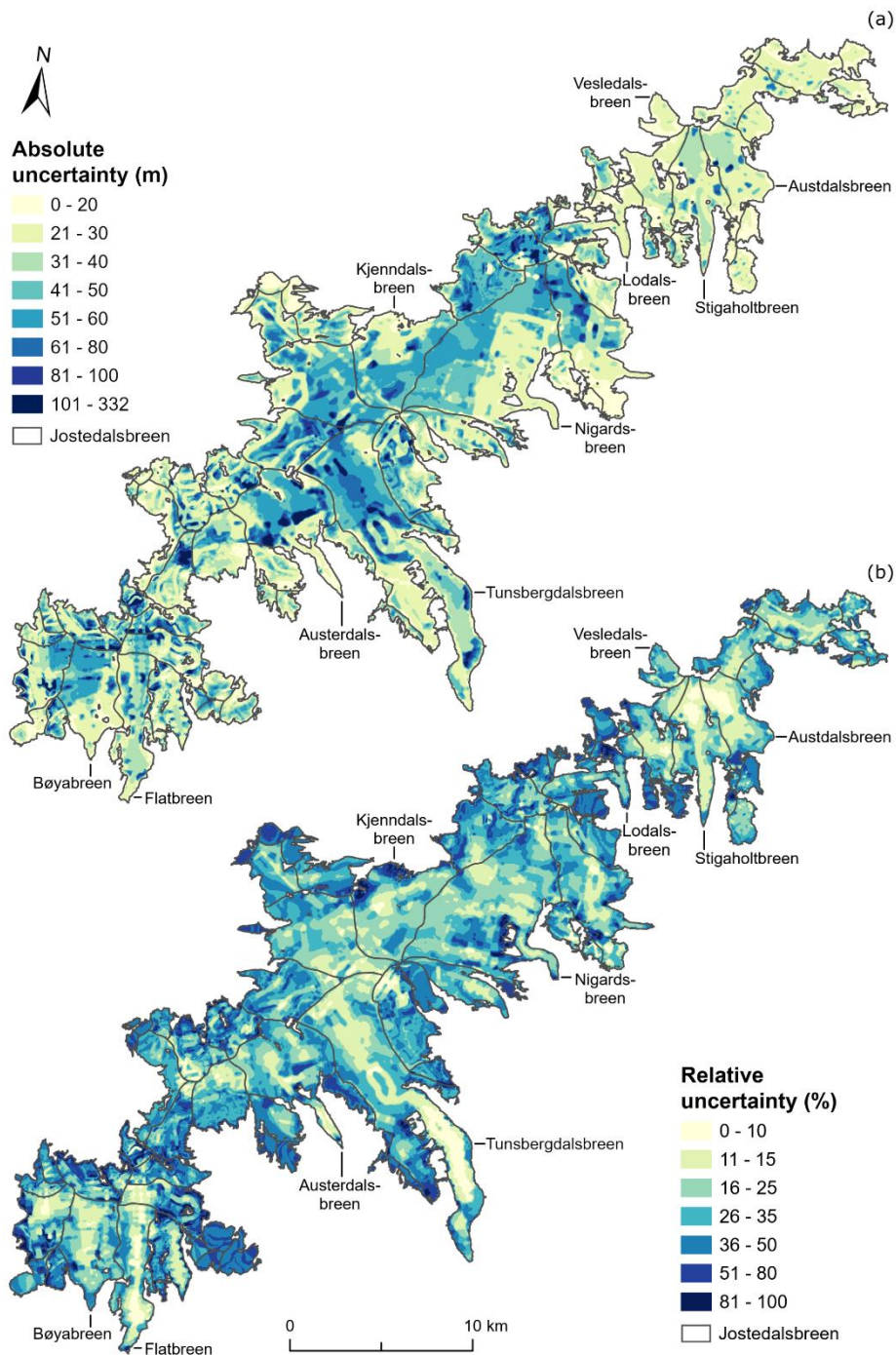
679

680



681

682 **Figure 9: (a) Modelled distributed 10 m ice thickness of Jostedalsgreen and (b) distributed 10 m bed topography**  
 683 **calculated from DTM10 and the modelled ice thickness distribution (Fig. 9a). The 2019 outlines of glacier units are from**  
 684 **Andreassen et al. (2022).**



685

686

687

688

689

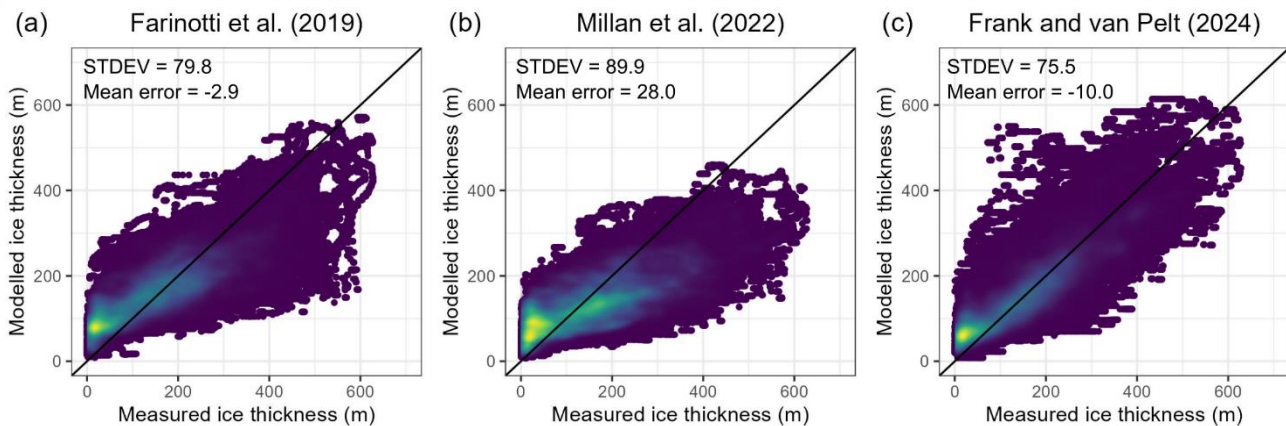
**Figure 10: (a) Absolute and (b) relative uncertainty for distributed ice thickness on Jostedalsgreen. The two figures illustrate that the largest absolute uncertainties appear in regions with thick ice and away from GPR profiles, while the largest relative uncertainties are found in the thin ice marginal regions. The 2019 outlines of glacier units are from Andreassen et al. (2022).**

690

691 Overall, the presented results are consistent with previous estimates of the volume and ice thickness distribution  
692 for Jostedalsbreen, and any smaller discrepancies are well within the uncertainty of the applied methodologies.  
693 The calculated mean ice thickness (154 m) is slightly smaller than the earlier estimate of 158 m which was  
694 calculated for an interpolated region covering 65 % (310 km<sup>2</sup>) of the 2006 area (474 km<sup>2</sup>) of Jostedalsbreen  
695 (Andreassen et al., 2015). Our calculated ice volume (70.6 km<sup>3</sup>) compares well with previous volume estimates of  
696 69.6 km<sup>3</sup> and 68.5 km<sup>3</sup> from global or regional studies provided by Farinotti et al. (2019) and Frank and van Pelt  
697 (2024) respectively, while the ice thickness model proposed by Millan et al. (2022) appears to underestimate the  
698 ice thickness at Jostedalsbreen, with a calculated volume of 56.5 km<sup>3</sup>. A comparison of our point thickness  
699 measurements with modelled values from the respective studies (Fig. 11), indicates a standard deviation of  
700 between 75 and 90 m. The mean error is small for Farinotti et al. (2019) and implies too small ice thicknesses for  
701 Millan et al. (2022) and somewhat too high ice thicknesses for Frank and van Pelt (2024).

702

703



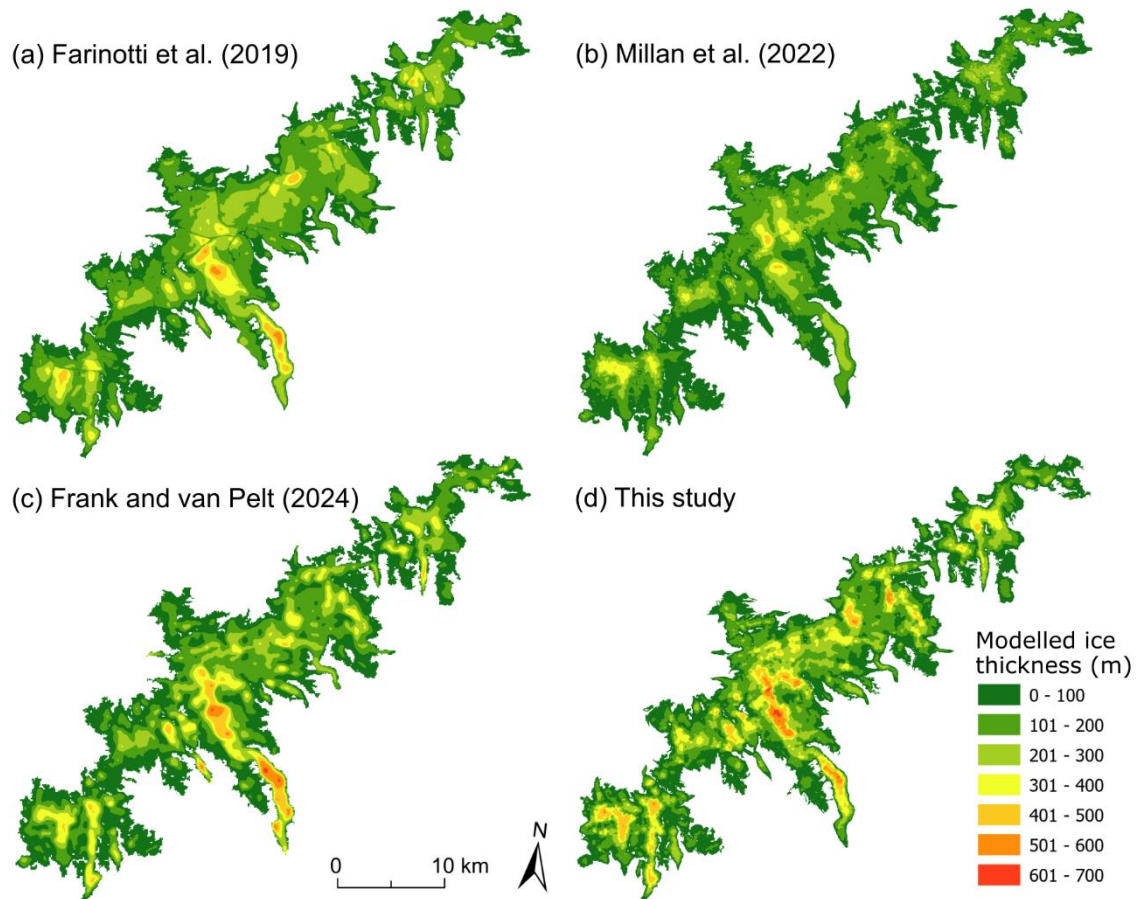
704

705 **Figure 11: Comparison of measured and modelled point ice thickness across Jostedalsbreen according to the large-**  
706 **scale ice thickness model datasets by (a) Farinotti et al. (2019), (b) Millan et al. (2022), and (c) Frank and van Pelt (2024).**  
707 **Comparisons are limited to locations within the respective model grid and calculated mean error (in meters) is negative**  
708 **when modelled ice thicknesses exceed measured ice thicknesses. Colours indicate point density and the black line in**  
709 **each figure shows the 1:1 line.**

710

711 Modelled ice thickness distribution shows that all large-scale ice thickness models capture the general pattern (Fig.  
712 12). However, the results of Farinotti et al. (2019) reveal unrealistic values along the ice divides (Fig. 12a), while  
713 the result by Millan et al. (2022) underestimates thickness both in glacial troughs and in the interior of the ice cap  
714 (Fig. 12b). The inferred thicknesses by Frank and van Pelt (2024) shows a tendency to overestimate thickness on  
715 outlet glacier tongues but in general shows an ice thickness distribution very consistent with our result (Fig. 12c).

716 Our comprehensive dataset of thickness measurements is expected to improve future regional to global-scale  
717 assessment of ice thickness distribution by supporting the calibration and validation of ice thickness models.  
718  
719



720  
721 **Figure 12: Ice thickness distribution on Jostedalsbreen according to the large-scale model studies by (a) Farinotti et**  
722 **al. (2019), (b) Millan et al. (2022), (c) Frank and van Pelt (2024), and (d) this study.**

723  
724 Calculations of key numbers for selected elements of the ice cap (Table 3) show that Jostedalsbreen Central is by  
725 far the largest of the three regions when comparing area, mean ice thickness and volume. The two surrounding  
726 regions have much smaller areas and ice is generally thinner, in particular in the smallest northernmost region. The  
727 ice thickness measurements presented in section 4.1 illustrate the vulnerability of Jostedalsbreen to future  
728 separation into three minor ice caps. Following a future breakup, Jostedalsbreen Central would remain the largest

729 glacier in Norway and mainland Europe, surpassing the second largest glacier, Vestre Svartisen, which had an  
 730 area of 192.2 km<sup>2</sup> in 2018 (Andreassen et al., 2022).

731

732 **Table 3: Key numbers for the three regions (North, Central and South) and prominent outlet glaciers based on**  
 733 **calculations from the model-based grid of ice thickness for Jostedalsbreen. The bracketed values after each glacier**  
 734 **name refer to glacier IDs from Andreassen and Winsvold (2012b). Data coverage is defined as all regions which are**  
 735 **less than 300 m from a point of known ice thickness (measurements or glacier outline), with bracketed values**  
 736 **specifying the percentage of the area which are less than 100 m from a known point.**

Glacier	Area (km <sup>2</sup> )	Maximum (m)	Mean (m)	Volume (km <sup>3</sup> )	Data coverage (%)
Jostedalsbreen	458.1	626	154	70.6	90 (49)
North	69.3	432	123	8.5	99 (69)
Central	309.6	626	161	49.9	88 (45)
South	79.3	518	155	12.3	91 (47)
Lodalsbreen (2266)	8.8	329	93	0.88	98 (57)
Kjenndalsbreen (2296)	19.1	419	186	3.6	92 (50)
Nigardsbreen (2297)	41.7	572	178	7.4	98 (62)
Nigardsbreen MB* (2311, 2299 and 2297)	45.4	572	169	7.6	98 (62)
Tunsbergdalsbreen (2320)	46.2	626	233	10.8	89 (45)
Austerdalsbreen (2327)	19.4	510	191	3.7	85 (44)
Bøyabreen (2349)	13.8	501	201	2.8	99 (53)
Flatbreen/Supphellebreen (2352)	12.7	452	205	2.68	97 (58)
Austdalsbreen (2478)	10.3	402	188	1.98	100 (70)
Stigaholtbreen (2480)	12.5	432	188	2.38	99 (65)

737 \*Nigardsbreen MB refers to the mass balance glacier basin used by Andreassen et al. (2023).

738

739 Beneath Jostedalsbreen we observe a versatile landscape of deep glacially incised valleys that extend to the centre  
 740 of the ice cap in some regions, and are surrounded by steep valley walls, hanging valleys and glacial over-  
 741 deepenings (Fig. 9b). The map of bed topography provides a glimpse of how the landscape would look if  
 742 Jostedalsbreen was to completely disappear and from it we can infer possible future changes in the regional  
 743 hydrological systems. While a detailed analysis of hydrological changes in the region is outside the scope of this  
 744 study, it is worth noting that several glaciers have discrepancies between the ice divides defined by the current  
 745 surface topography of the ice cap and the hydrological catchment boundaries determined by the bed topography  
 746 in an ice-free landscape. Examples of such are Flatbreen/Supphellebreen, Tunsbergdalsbreen and Nigardsbreen,  
 747 where the subglacial valleys appear to extend significantly beyond the current ice divides (Fig. 9b). Other glaciers,

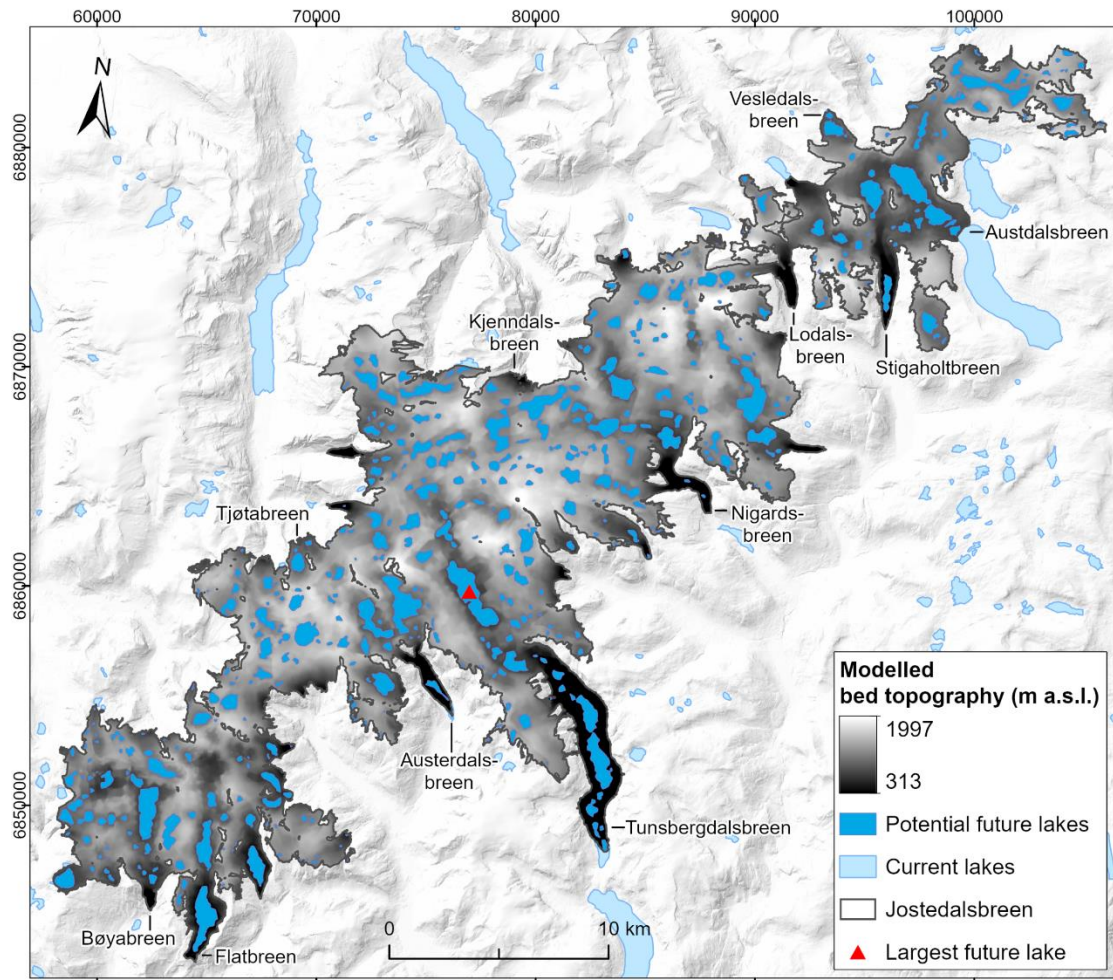
748 such as at Austerdalsbreen and Lodalsbreen, have matching surface and subglacial topographical divides. Overall,  
749 it appears likely that in an ice-free landscape, upper catchment boundaries in the central and southern  
750 Jostedalbreen regions will, in many places, be located further north and northwest than the currently more central  
751 longitudinal ice divide. In the northern parts of Jostedalbreen, the potential extent of ice-free catchment areas  
752 appears more uncertain due to several smaller thresholds in the bed topography and limitations in data coverage  
753 across these. Consequently, we tentatively suggest that in an ice-free landscape, the topographic bed catchment  
754 at Austdalsbreen may increase substantially in size at the expense of the surrounding regions, although further  
755 analysis is required to substantiate this claim.

756

757 The distributed bed topography furthermore reveals subglacial bed depressions as likely locations for future lakes  
758 in a warming climate (Fig. 13). Our results show a multitude of potential lakes, the largest of which is 3.5 km long,  
759 has an area of 2.4 km<sup>2</sup> and is located in the inner regions of Tunsbergdalsbreen, just south of where the thickest  
760 ice was measured. Other large topographic depressions are found north of Bøyabreen and Flatbreen glacier fronts,  
761 underneath the glacier tongue of Tunsbergdalsbreen, and north-west of the calving front of Austdalsbreen.  
762 According to our estimates, a total of 14 % (65.3 km<sup>2</sup>) of the present-day glacier area of 458 km<sup>2</sup> (2019) can be  
763 covered by lakes if the entire Jostedalbreen melts away.

764





765

766

767

768

769

770

771

772

**Figure 13: Location of current and potential future lakes calculated from the grid of subglacial bed topography at Jostedalsgreen (Fig. 9b). The largest potential future lake is marked by a red triangle. The 2019 outline of Jostedalsgreen is from Andreassen et al. (2022) and the background mountain shadow and outlines are from the Norwegian Mapping Authority. Outline of present-day lakes is from the Norwegian Mapping Authority (WMS for Topografisk Norgeskart available at <https://www.geonorge.no/>) and the Norwegian Water Resources and Energy Directorate (<https://doi.org/10.1017/jog.2022.20>). The coordinate system is UTM 33N, datum ETRS\_1989.**

## 773 **5 Data availability**

774 All ice thickness observations (complete and thinned-out compilations) and maps of ice cap-wide ice thickness,  
775 combined uncertainty in ice thickness, bed topography and outlines of potential future lakes are available for  
776 download at <https://doi.org/10.58059/yhwr-rx55> which is hosted by the Norwegian Nasjonalt Vitenarkiv (Gillespie  
777 et al., 2024).

## 778 **6 Conclusions**

779 In this paper, we present a rich point dataset of high-quality ice thickness observations on Jostedalsbreen ice cap  
780 collected during GPR surveys in 2018–2023. Measurements were collected from 59 of the 81 glacier units that  
781 constitute Jostedalsbreen and 90 % of the total ice cap area is now less than 300 m from a point of known ice  
782 thickness. A maximum ice thickness of ~630 m was measured on Tunsbergdalsbreen in the central part of the ice  
783 cap. This measurement exceeds the 600 m maximum thickness previously measured on Jostedalsbreen (Sætrang  
784 and Wold, 1986; Andreassen et al., 2015). Smaller maximum ice thicknesses of ~520 m and ~430 m were  
785 measured in the southern and northern regions of the ice cap, respectively. Using this new dataset of ice thickness  
786 values, we produce model-based grids of distributed ice thickness and bed topography that allow for a coherent  
787 description of ice thickness variations and subglacial morphology over the entire Jostedalsbreen (458 km<sup>2</sup>), as well  
788 as calculations of key figures for the ice cap. We find that Jostedalsbreen has a present (~2020) mean thickness  
789 of 154 m ±22 m and an ice volume of 70.6 ±10.2 km<sup>3</sup>. Together, the ice thickness measurements and distributed  
790 datasets provide exceptional new details about the geometry and bed topography of Jostedalsbreen, revealing  
791 vulnerabilities to future ice cap fragmentation and possible changes in the hydrological systems with climate  
792 warming. These datasets will be of particular value to future climate change impact studies in the Jostedalsbreen  
793 region, which are of high importance to local stakeholders such as farmers, tourist operators and hydropower  
794 companies.

## 795 **Author contributions**

796 MKG, JCY, and LMA designed the study. MKG led the data collection of ice thickness measurements and MKG,  
797 SDV, KHS, JA, JB, JMC, HE, BK, EL, MM, KM, SDN, TOR, EWNS and KØ carried out the fieldwork. MKG  
798 subsequently processed and interpreted the ice thickness data. MH ran the model-based extrapolation of ice  
799 thickness measurements and prepared all distributed datasets while MKG, LMA and KHS produced the figures.  
800 MKG, LMA and MH prepared the manuscript with contributions from all co-authors. JCY was the principal  
801 investigator of the JOSTICE project.

802

## 803 **Acknowledgements**

804 We would like to express our sincere gratitude to all who have contributed to the planning and implementation of  
805 the comprehensive and challenging fieldwork that was required to adequately map ice thickness across  
806 Jostedalsgreen. Especially, we would like to thank Marthe Gjerde, Henning Åkesson and Ingebjørg Haugland for  
807 assisting during the 2021 field campaign and Jostedalsgreen National Park, Nigardsbreen Nature Reserve,  
808 Breheimen National Park and the municipalities of Luster, Stryn, Sogndal, Sunnfjord and Skjåk who all granted  
809 permissions for the fieldwork. We would also like to thank Airlift AS who provided logistical support during both  
810 ground-based and airborne radar surveys. Steinmannen and Statkraftthytta mountain huts, both owned by Statkraft,  
811 generously accommodated us during the fieldwork and snowmobiles were provided by Vang Auto-Service AS,  
812 Luster Red Cross mountain rescue group and Statkraft. Lastly, we thank Statkraft for advising on weather  
813 conditions and NVE for their local avalanche forecasting.

## 814 **Competing interests**

815 All co-authors other than EL declare that they have no conflict of interest. EL works for the hydropower company  
816 Statkraft, and Statkraft has an interest in the hydropower production at Austdalsgreen. Statkraft did not in any way  
817 influence the research objectives, data collection, analysis or interpretations of data presented in this paper.

## 818 **Financial support**

819 This study is a contribution to the JOSTICE project funded by the Norwegian Research Council (RCN grant  
820 #302458). In addition, the 2023 airborne survey was supported by funding from UH-nett Vest.

## 821 **References**

- 822 Andreassen, Elvehøy, H., Kjøllmoen, B., Engeset, R. V. and Haakensen, N.: Glacier mass balance and length  
823 variation in Norway, *Ann. Glaciol.*, 42, 317–325, 10.3189/172756405781812826, 2005.  
824
- 825 Andreassen, L. M., Melvold, K., Nordli, Ø., Nordli, Ø., and Rasmussen, A.: Langfjordjøkelen, a rapidly shrinking  
826 glacier in northern Norway, *J. Glaciol.*, 58, 581–593, 10.3189/2012JoG11J014, 2012a.  
827
- 828 Andreassen, L. M. and Winsvold, S. H. (eds), Paul, F. and Hausberg, J. E.: Inventory of Norwegian Glaciers, NVE  
829 report 38-2012. Norwegian Water Resources and Energy Directorate, Oslo, Norway, 2012b.  
830
- 831 Andreassen, L. M., Elvehøy, H., Huss, M., Melvold, K., and Winsvold, S. H.: Ice thickness measurements and  
832 volume estimates for glaciers in Norway, *J. Glaciol.*, 61, 763–775, 10.3189/2015JoG14J161, 2015.  
833

834 Andreassen, L. M., Nagy, T., Kjølmoen, B., and Leigh, J. R.: An inventory of Norway's glaciers and ice-marginal  
835 lakes from 2018–19 Sentinel-2 data, *J. Glaciol.*, 68, 1085–1106, 10.1017/jog.2022.20, 2022.

836

837 Andreassen, L. M., Carrivick, J. L., Elvehøy, H., Kjølmoen, B., Robson, B. A., and Sjrursen, K. H.: Spatio-temporal  
838 variability in geometry and geodetic mass balance of Jostedalbreen ice cap, Norway, *Ann. Glaciol.*, 1–18,  
839 10.1017/aog.2023.70, 2023.

840

841 Binder, D., Brückl, E., Roch, K. H., Behm, M., Schöner, W., and Hynek, B.: Determination of total ice volume and  
842 ice-thickness distribution of two glaciers in the Hohe Tauern region, Eastern Alps, from GPR data, *Ann. Glaciol.*,  
843 50, 71–79, 2009.

844

845 Bolibar, J., Rabatel, A., Gouttevin, I., Zekollari, H., and Galiez, C.: Nonlinear sensitivity of glacier mass balance to  
846 future climate change unveiled by deep learning, *Nat. Commun.*, 13, 409, 2022.

847

848 Carrivick, J. L., Andreassen, L. M., Nesje, A., and Yde, J. C.: A reconstruction of Jostedalbreen during the Little  
849 Ice Age and geometric changes to outlet glaciers since then, *Quat. Sci. Rev.*, 284, 107501,  
850 <https://doi.org/10.1016/j.quascirev.2022.107501>, 2022.

851

852 Dowdeswell, J. A. and Evans, S.: Investigations of the form and flow of ice sheets and glaciers using radio-echo  
853 sounding, *Rep. Prog. Phys.*, 67, 1821, 10.1088/0034-4885/67/10/R03, 2004.

854

855 Engen, S. H., Gjerde, M., Scheiber, T., Seier, G., Elvehøy, H., Abermann, J., Nesje, A., Winkler, S., Hualand, K.  
856 F., Rütther, D. C., Maschler, A., Robson, B. A., and Yde, J. C.: Investigation of the 2010 rock avalanche onto the  
857 regenerated glacier Brenndalsbreen, Norway, *Landslides*, 21, 2051–2072, 10.1007/s10346-024-02275-z, 2024.

858

859 Engeset, R. V., Jackson, M., and Schuler, T. V.: Analysis of the first jökulhlaup at Blåmannsisen, northern Norway,  
860 and implications for future events, *Ann. Glaciol.*, 42, 35–41, 10.3189/172756405781812600, 2005.

861

862 Farinotti, D., Huss, M., Bauder, A., Funk, M., and Truffer, M.: A method to estimate the ice volume and ice-thickness  
863 distribution of alpine glaciers, *J. Glaciol.*, 55, 422–430, 2009.

864

865 Farinotti, D., Brinkerhoff, D. J., Clarke, G. K. C., Fürst, J. J., Frey, H., Gantayat, P., Gillet-Chaulet, F., Girard, C.,  
866 Huss, M., Leclercq, P. W., Linsbauer, A., Machguth, H., Martin, C., Maussion, F., Morlighem, M., Mosbeux, C.,  
867 Pandit, A., Portmann, A., Rabatel, A., Ramsankaran, R., Reerink, T. J., Sanchez, O., Stenoft, P. A., Singh Kumari,  
868 S., van Pelt, W. J. J., Anderson, B., Benham, T., Binder, D., Dowdeswell, J. A., Fischer, A., Helfricht, K., Kutuzov,  
869 S., Lavrentiev, I., McNabb, R., Gudmundsson, G. H., Li, H., and Andreassen, L. M.: How accurate are estimates  
870 of glacier ice thickness? Results from ITMIX, the Ice Thickness Models Intercomparison eXperiment, *Cryosphere*,  
871 11, 949–970, 10.5194/tc-11-949-2017, 2017.

872

873 Farinotti, D., Huss, M., Fürst, J. J., Landmann, J., Machguth, H., Maussion, F., and Pandit, A.: A consensus  
874 estimate for the ice thickness distribution of all glaciers on Earth, *Nat. Geosci.*, 12, 168–173, 10.1038/s41561-019-  
875 0300-3, 2019.

876

877 Farinotti, D., Brinkerhoff, D. J., Fürst, J. J., Gantayat, P., Gillet-Chaulet, F., Huss, M., Leclercq, P. W., Maurer, H.,  
878 Morlighem, M., Pandit, A., Rabatel, A., Ramsankaran, R., Reerink, T. J., Robo, E., Rouges, E., Tamre, E., van Pelt,  
879 W. J. J., Werder, M. A., Azam, M. F., Li, H., and Andreassen, L. M.: Results from the ice thickness models  
880 intercomparison experiment phase 2 (ITMIX2), *Front. Earth Sci.*, 8, 571923, 2021.

881

882 Fischer, A.: Calculation of glacier volume from sparse ice-thickness data, applied to Schaufelferner, Austria, *J.*  
883 *Glaciol.*, 55, 453–460, 10.3189/002214309788816740, 2009.

884  
885 Flowers, G. E. and Clarke, G. K. C.: Surface and bed topography of Trapridge Glacier, Yukon Territory, Canada:  
886 digital elevation models and derived hydraulic geometry, *J. Glaciol.*, 45, 165–174, 10.3189/S0022143000003142,  
887 1999.  
888  
889 Frank, T., van Pelt, W. J. J., and Kohler, J.: Reconciling ice dynamics and bed topography with a versatile and fast  
890 ice thickness inversion, *Cryosphere*, 17, 4021–4045, 10.5194/tc-17-4021-2023, 2023.  
891  
892 Frank, T., and van Pelt, W. J. J.: Ice volume and thickness of all Scandinavian glaciers and ice caps, *J. Glaciol.*,  
893 1–34, 10.1017/jog.2024.25, 2024.  
894  
895 Frémand, A. C., Fretwell, P., Bodart, J. A., Pritchard, H. D., Aitken, A., Bamber, J. L., Bell, R., Bianchi, C., Bingham,  
896 R. G., Blankenship, D. D., Casassa, G., Catania, G., Christianson, K., Conway, H., Corr, H. F. J., Cui, X., Damaske,  
897 D., Damm, V., Drews, R., Eagles, G., Eisen, O., Eisermann, H., Ferraccioli, F., Field, E., Forsberg, R., Franke, S.,  
898 Fujita, S., Gim, Y., Goel, V., Gogineni, S. P., Greenbaum, J., Hills, B., Hindmarsh, R. C. A., Hoffman, A. O.,  
899 Holmlund, P., Holschuh, N., Holt, J. W., Horlings, A. N., Humbert, A., Jacobel, R. W., Jansen, D., Jenkins, A., Joket,  
900 W., Jordan, T., King, E., Kohler, J., Krabill, W., Kusk Gillespie, M., Langley, K., Lee, J., Leitchenkov, G., Leuschen,  
901 C., Luyendyk, B., MacGregor, J., MacKie, E., Matsuoka, K., Morlighem, M., Mouginot, J., Nitsche, F. O., Nogi, Y.,  
902 Nost, O. A., Paden, J., Pattyn, F., Popov, S. V., Rignot, E., Rippin, D. M., Rivera, A., Roberts, J., Ross, N., Ruppel,  
903 A., Schroeder, D. M., Siegert, M. J., Smith, A. M., Steinhage, D., Studinger, M., Sun, B., Tabacco, I., Tinto, K.,  
904 Urbini, S., Vaughan, D., Welch, B. C., Wilson, D. S., Young, D. A., and Zirizzotti, A.: Antarctic Bedmap data:  
905 Findable, Accessible, Interoperable, and Reusable (FAIR) sharing of 60 years of ice bed, surface, and thickness  
906 data, *Earth Syst. Sci. Data*, 15, 2695–2710, 10.5194/essd-15-2695-2023, 2023.  
907  
908 Fürst, J. J., Gillet-Chaulet, F., Benham, T. J., Dowdeswell, J. A., Grabiec, M., Navarro, F., Pettersson, R., Moholdt,  
909 G., Nuth, C., and Sass, B.: Application of a two-step approach for mapping ice thickness to various glacier types  
910 on Svalbard, *Cryosphere*, 11, 2003–2032, 2017.  
911  
912 Gärtner-Roer, I., Naegeli, K., Huss, M., Knecht, T., Machguth, H., and Zemp, M.: A database of worldwide glacier  
913 thickness observations, *Glob. Planet. Change.*, 122, 330–344, <https://doi.org/10.1016/j.gloplacha.2014.09.003>,  
914 2014.  
915  
916 Giesen, R. H. and Oerlemans, J.: Response of the ice cap Hardangerjøkulen in southern Norway to the 20th and  
917 21st century climates, *Cryosphere*, 4, 191–213, 10.5194/tc-4-191-2010, 2010.  
918  
919 Gillespie, M. K., Yde, J. C., Andresen, M. S., Citterio, M., and Gillespie, M. A. K.: Ice geometry and thermal regime  
920 of Lyngmarksbræen Ice Cap, West Greenland, *J. Glaciol.*, 1–13, 10.1017/jog.2023.89, 2023.  
921  
922 Gillespie, M. K., Andreassen, L. M., Huss, M., de Villiers, S., Sjursen, K. H., Aasen, J., Bakke, J., Cederstrøm, J.  
923 M., Elvehøy, H., Kjølmoen, B., Loe, E., Meland, M., Melvold, K., Nerhus, S. D., Røthe, T. O., Støren, E. W. N.,  
924 Øst, K., and Yde, J. C.: Jostedalbreen ice thickness and bed topography [dataset], 10.58059/yhwr-rx55, 2024.  
925  
926 GlaThiDa Consortium: Glacier Thickness Database 3.1.0, World Glacier Monitoring Service, Zurich, Switzerland,  
927 10.5904/wgms-glathida-2020-10, 2020.  
928  
929 Glen, J. W.: The creep of polycrystalline ice, *Proceedings of the Royal Society of London. Series A. Mathematical*  
930 *and Physical Sciences*, 228, 519–538, 1955.  
931

932 Grab, M., Mattea, E., Bauder, A., Huss, M., Rabenstein, L., Hodel, E., Linsbauer, A., Langhammer, L., Schmid, L.,  
933 and Church, G.: Ice thickness distribution of all Swiss glaciers based on extended ground-penetrating radar data  
934 and glaciological modeling, *J. Glaciol.*, 67, 1074–1092, 2021.

935

936 Gudmundsson, G. H.: Transmission of basal variability to a glacier surface, *J. Geophys. Res.*, 108, 2253,  
937 10.1029/2002JB002107, 2003.

938

939 Huss, M. and Farinotti, D.: Distributed ice thickness and volume of all glaciers around the globe, *J. Geophys. Res.*  
940 *Earth Surf.*, 117, 2012.

941

942 Huss, M. and Farinotti, D.: A high-resolution bedrock map for the Antarctic Peninsula, *Cryosphere*, 8, 1261–1273,  
943 2014.

944

945 Haakensen, N. and Wold, B.: Breheimen-Stryn: Undersøkelse av bunntopografi på Bødalsbreen, *NVE Rapp.*, 17–  
946 86, 1986.

947

948 IPCC: *Climate Change 2021: The Physical Science Basis. Contribution of Working Group I to the Sixth Assessment*  
949 *Report of the Intergovernmental Panel on Climate Change*, 2021.

950

951 Johansson, F. E., Bakke, J., Støren, E. N., Gillespie, M. K., and Laumann, T.: Mapping of the Subglacial  
952 Topography of Folgefonna Ice Cap in Western Norway—Consequences for Ice Retreat Patterns and Hydrological  
953 Changes, *Front. Earth Sci.*, 10, 10.3389/feart.2022.886361, 2022.

954

955 Kennett M.: Kartlegging av istykkelse og feltavgrensning på Spørteggbreen 1989, *NVE Rapp.* 15-1989,  
956 oppdragsrapport1989\_15.pdf (nve.no), 1989.

957

958 Kennett M.: Kartlegging av istykkelse og feltavgrensning på Blåmannsisen 1990, *NVE Rapp.* 8-1990  
959 oppdragsrapport1990\_08.pdf (nve.no), 1990.

960

961 Kjøllmoen, B., Andreassen, L.M. and Elvehøy H.: Glaciological investigations in Norway 2023, *NVE Rapp.* 22-  
962 2024, 2024.

963

964 Lapazaran, J. J., Martín-Español, A., Navarro, F. J., and Otero, J.: On the errors involved in ice-thickness estimates  
965 I: ground-penetrating radar measurement errors, *J. Glaciol.*, 62, 1008–1020, 10.1017/jog.2016.93, 2016.

966

967 Laumann, T. and Nesje, A.: The impact of climate change on future frontal variations of Briksdalsbreen, western  
968 Norway, *J. Glaciol.*, 55, 789–796, 10.3189/002214309790152366, 2009.

969

970 Laumann, T. and Nesje, A.: Spørteggbreen, western Norway, in the past, present and future: Simulations with a  
971 two-dimensional dynamical glacier model, *Holocene*, 24, 842–852, 10.1177/0959683614530446, 2014.

972

973 Lindbäck, K., Kohler, J., Pettersson, R., Nuth, C., Langley, K., Messerli, A., Vallot, D., Matsuoka, K., and Brandt,  
974 O.: Subglacial topography, ice thickness, and bathymetry of Kongsfjorden, northwestern Svalbard, *Earth Syst. Sci.*  
975 *Data*, 10, 1769–1781, 10.5194/essd-10-1769-2018, 2018.

976

977 Linsbauer, A., Paul, F., and Haeberli, W.: Modeling glacier thickness distribution and bed topography over entire  
978 mountain ranges with GlabTop: Application of a fast and robust approach, *J. Geophys. Res. Earth Surf.*, 117, 2012.

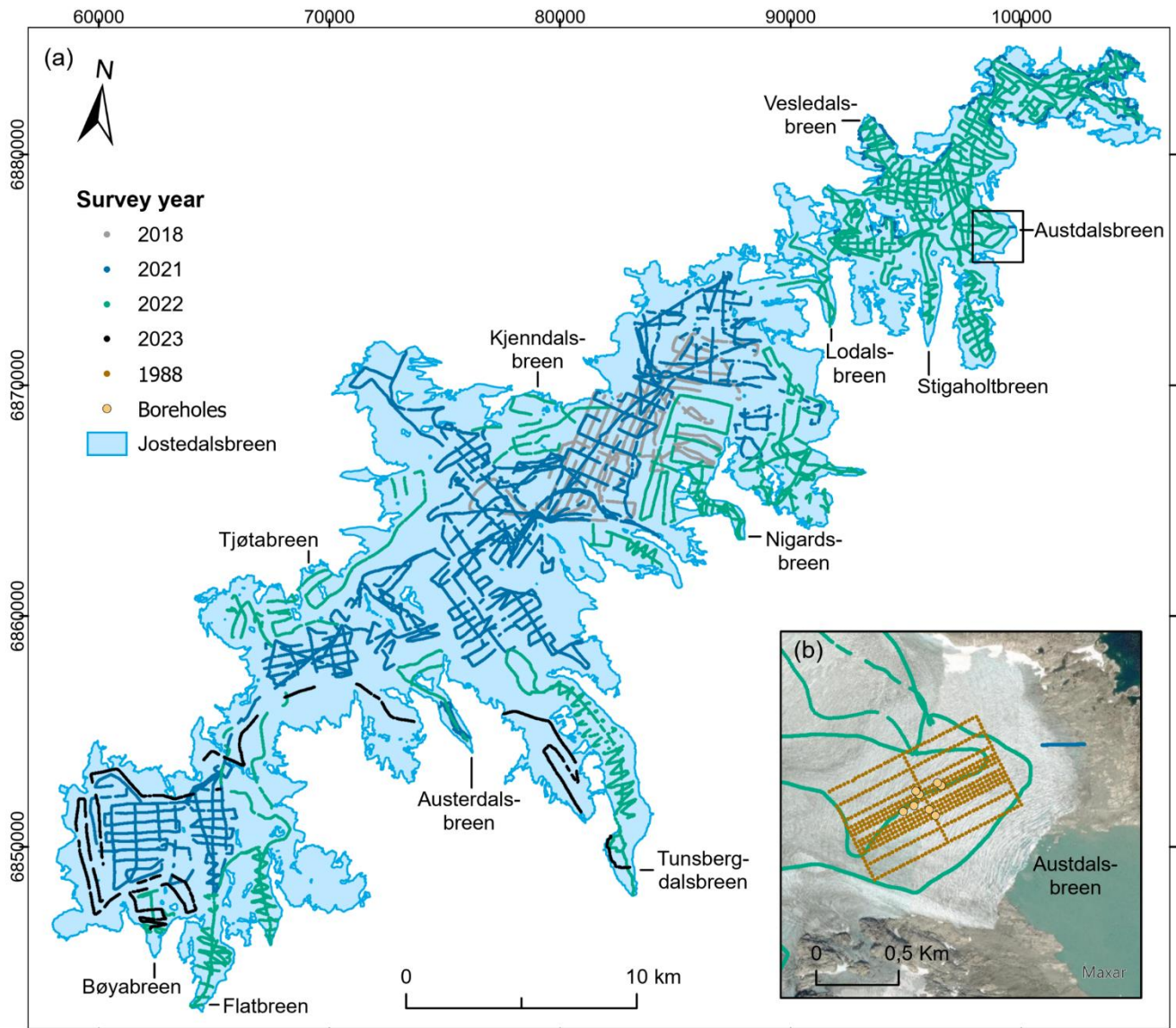
979

980 Millan, R., Mouginot, J., Rabatel, A., and Morlighem, M.: Ice velocity and thickness of the world's glaciers, *Nat.*  
981 *Geosci.*, 15, 124–129, 10.1038/s41561-021-00885-z, 2022.

982  
983 Mingo, L. and Flowers, G. E.: An integrated lightweight ice-penetrating radar system, *J. Glaciol.*, 56, 709–714,  
984 10.3189/002214310793146179, 2010.  
985  
986 Morlighem, M., Williams, C. N., Rignot, E., An, L., Arndt, J. E., Bamber, J. L., Catania, G., Chauché, N., Dowdeswell,  
987 J. A., Dorschel, B., Fenty, I., Hogan, K., Howat, I., Hubbard, A., Jakobsson, M., Jordan, T. M., Kjeldsen, K. K.,  
988 Millan, R., Mayer, L., Mouginot, J., Noël, B. P. Y., O’Cofaigh, C., Palmer, S., Rysgaard, S., Seroussi, H., Siegert,  
989 M. J., Slabon, P., Straneo, F., van den Broeke, M. R., Weinrebe, W., Wood, M. and Zinglensen, K. B.: BedMachine  
990 v3: Complete bed topography and ocean bathymetry mapping of Greenland from multibeam echo sounding  
991 combined with mass conservation, *Geophys. Res. Lett.*, 44, 11,051–11,061. 10.1002/2017GL074954, 2017.  
992  
993 Navarro, F. and Eisen, O.: Ground-penetrating radar in glaciological applications, in: Remote sensing of glaciers:  
994 Techniques for topographic, spatial and thematic mapping of glaciers, Taylor & Francis London, 195–229, 2009.  
995  
996 Nesje, A., Johannessen, T., and Birks, H. J. B.: Briksdalsbreen, western Norway: climatic effects on the terminal  
997 response of a temperate glacier between AD 1901 and 1994, *Holocene*, 5, 343–347,  
998 10.1177/095968369500500310, 1995.  
999  
1000 Ogier, C., van Manen, D.-J., Maurer, H., Räss, L., Hertrich, M., Bauder, A., and Farinotti, D.: Ground penetrating  
1001 radar in temperate ice: englacial water inclusions as limiting factor for data interpretation, *J. Glaciol.*, 1–12, 2023.  
1002  
1003 Paul F., Andreassen L.M., and Winsvold S.H.: A new glacier inventory for the Jostedalbreen region, Norway, from  
1004 Landsat TM scenes of 2006 and changes since 1966, *Ann. Glaciol.*, 52, 153-162, 10.3189/172756411799096169,  
1005 2011.  
1006  
1007 Pettersson, R., Christoffersen, P., Dowdeswell, J. A., Pohjola, V. A., Hubbard, A., and Strozzi, T.: Ice thickness  
1008 and basal conditions of Vestfonna ice cap, eastern Svalbard, *Geogr. Ann. A: Phys. Geogr.*, 93, 311–322, 2011.  
1009  
1010 Plewes, L. A. and Hubbard, B.: A review of the use of radio-echo sounding in glaciology, *Prog. Phys. Geogr.*, 25,  
1011 203–236, 2001.  
1012  
1013 Rounce, D. R., Hock, R., Maussion, F., Hugonnet, R., Kochtitzky, W., Huss, M., Berthier, E., Brinkerhoff, D.,  
1014 Compagno, L., and Copland, L.: Global glacier change in the 21st century: Every increase in temperature matters,  
1015 *Science*, 379, 78–83, 2023.  
1016  
1017 Schlegel, R., Kulesa, B., Murray, T., and Eisen, O.: Towards a common terminology in radioglaciology, *Ann.*  
1018 *Glaciol.*, 63, 8–12, 2022.  
1019  
1020 Seier, G., Abermann, J., Andreassen, L. M., Carrivick, J. L., Kielland, P. H., Löffler, K., Nesje, A., Robson, B. A.,  
1021 Røthe, T. O., Scheiber, T., Winkler, S. and Yde, J. C.: Glacier thinning, recession and advance, and the associated  
1022 evolution of a glacial lake between 1966 and 2021 at Austerdalsbreen, western Norway, *Land. Degrad. Dev.*, 2024.  
1023  
1024 Sellevold, M. and Kloster, K.: Seismic measurements on the glacier Hardangerjøkulen, Western Norway, *Nor.*  
1025 *Polarinst. Årb.*, 87–91, 1964.  
1026  
1027 Smith, B. E. and Evans, S.: Radio echo sounding: absorption and scattering by water inclusion and ice lenses, *J.*  
1028 *Glaciol.*, 11, 133–146, 1972.  
1029  
1030 Sverrisson, M., Jóhannesson, Æ., and Björnsson, H.: Instruments and Methods: Radio-Echo Equipment for Depth  
1031 Sounding of Temperate Glaciers, *J. Glaciol.*, 25, 477–486, 1980.

- 1032  
1033 Sætrang, A. C.: Istykkelsesmålinger med breradar på Austdalsbreen, Heli-Anlegg Rapp., 5–88, 1988.  
1034  
1035 Sætrang, A. C. and Holmqvist, E.: Kartlegging av istykkelse på nordre Jostedalsbreen, NVE Rapp., 8-1987, 1987.  
1036  
1037 Sætrang, A. C. and Wold, B.: Results from the radio echo-sounding on parts of the Jostedalsbreen ice cap, Norway,  
1038 Ann. Glaciol., 8, 156–158, 1986.  
1039  
1040 Terratec: Laserskanning for nasjonal detaljert høydemodell, NDH Jostedalsbreen 2pkt, 2020.  
1041  
1042 Welty, E., Zemp, M., Navarro, F., Huss, M., Fürst, J. J., Gärtner-Roer, I., Landmann, J., Machguth, H., Naegeli, K.,  
1043 and Andreassen, L. M.: Worldwide version-controlled database of glacier thickness observations, Earth Syst. Sci.  
1044 Data., 12, 3039–3055, 2020.  
1045  
1046 Yde, J. C., Gillespie, M. K., Løland, R., Ruud, H., Mernild, S. H., Villiers, S. D., Knudsen, N. T., and Malmros, J. K.:  
1047 Volume measurements of Mittivakkat Gletscher, southeast Greenland, J. Glaciol., 60, 1199–1207, 2014.  
1048  
1049 Østrem, G., Liestøl, O., and Wold, B.: Glaciological investigations at Nigardsbreen, Norway, Nor. Geogr. Tidsskr.,  
1050 30, 187–209, 10.1080/00291957608552005, 1976.  
1051  
1052 Åkesson, H., Nisancioglu, K. H., Giesen, R. H., and Morlighem, M.: Simulating the evolution of Hardangerjøkulen  
1053 ice cap in southern Norway since the mid-Holocene and its sensitivity to climate change, Cryosphere, 11, 281–  
1054 302, 2017.  
1055  
1056





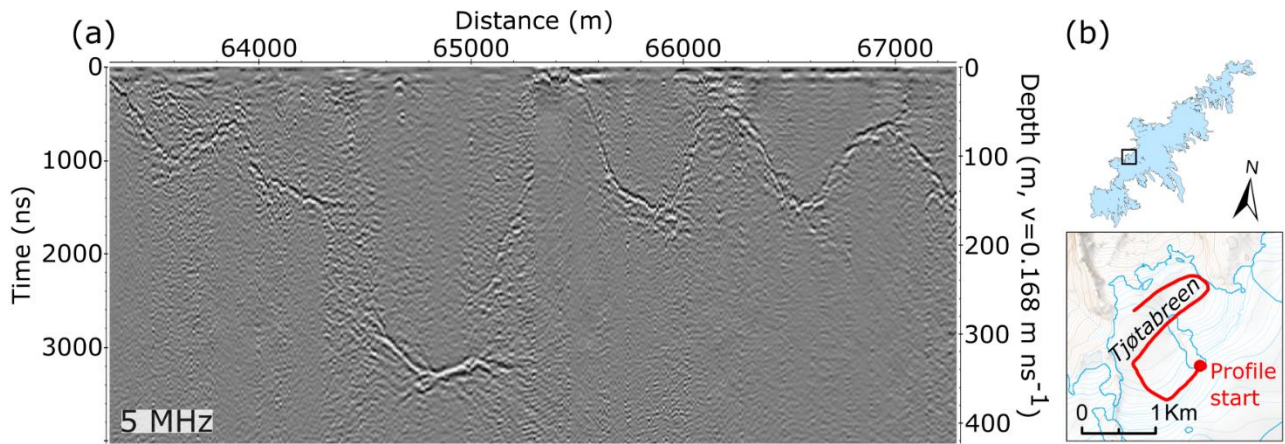
1061 **Figure A1: (a) Locations of ice thickness measurements divided into survey year, and (b) ice thickness measurements**  
 1062 **on Austdalsbreen, including the locations of the 1988 survey lines and boreholes from 1986 and 1987. The coordinate**  
 1063 **system on both maps is UTM 33N, datum ETRS89. The background imagery in (b) is from Esri**  
 1064 **([https://services.arcgisonline.com/ArcGIS/rest/services/World\\_Imagery/MapServer](https://services.arcgisonline.com/ArcGIS/rest/services/World_Imagery/MapServer)) and in this area relies on a Maxar**  
 1065 **mosaic with images from 2019 and 2021.**

1067 **Appendix B**

1068

1069

1070



1071

1072

1073

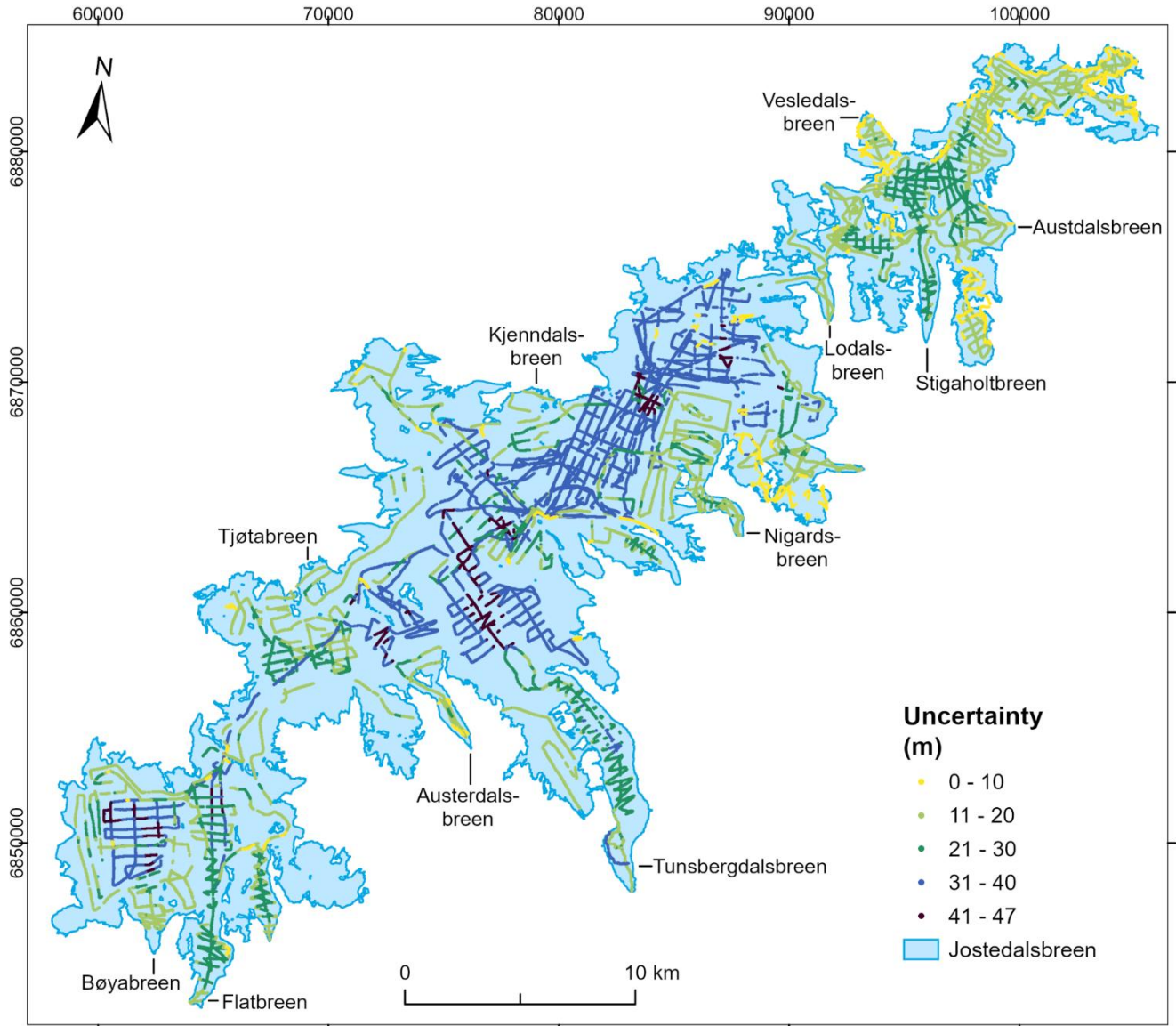
1074

1075

**Figure B1: (a) Example of measurements with the 5 MHz airborne radar system. (b) The profile was located along a transect at Tjøtabreen (Fig. 1). The background map in (b) is from the Norwegian Mapping Authority (WMS for Topografisk Norgeskart available at <https://www.geonorge.no/>) and the 2019 glacier outlines are from Andreassen et al. (2022).**

1076

1077



1079  
1080 **Figure C1: Total measurement uncertainty associated with each ice thickness observation calculated using the method**  
1081 **described by Lapazaran et al. (2016). The coordinate system is UTM 33N, datum ETRS89.**